The Astrophysical Journal, 964:79 (20pp), 2024 March 20 https://doi.org/10.3847/1538-4357/ad0974

Jets with a Twist: The Emergence of FR0 Jets in a 3D GRMHD Simulation of Zero-angular-momentum Black Hole Accretion

Aretaios Lalakos[1], Alexander Tchekhovskoy[1], Omer Bromberg[2], Ore Gottlieb[1,3,4], Jonatan Jacquemin-Ide[1], Matthew Liska[5,6], and Haocheng Zhang[7,8]
[1] Center for Interdisciplinary Exploration & Research in Astrophysics (CIERA), Physics & Astronomy, Northwestern University, Evanston, IL 60202, USA; lalakos@u.northwestern.edu
[2] The Raymond and Beverly Sackler School of Physics and Astronomy, Tel Aviv University, Tel Aviv 69978, Israel
[3] Center for Computational Astrophysics, Flatiron Institute, New York, NY 10010, USA
[4] Department of Physics and Columbia Astrophysics Laboratory, Columbia University, Pupin Hall, New York, NY 10027, USA
[5] Center for Relativistic Astrophysics, Georgia Institute of Technology, Howey Physics Bldg, 837 State Street NW, Atlanta, GA 30332, USA
[6] Institute for Theory and Computation, Harvard University, 60 Garden Street, Cambridge, MA 02138, USA
[7] Center for Space Sciences and Technology, University of Maryland Baltimore County, Baltimore, MD 21250, USA
[8] NASA Goddard Space Flight Center, Greenbelt, MD 20771, USA
Received 2023 October 18; revised 2023 October 26; accepted 2023 October 27; published 2024 March 19

Abstract

Spinning supermassive black holes (BHs) in active galactic nuclei magnetically launch relativistic collimated outflows, or jets. Without angular momentum supply, such jets are thought to perish within 3 orders of magnitude in distance from the BH, well before reaching kiloparsec scales. We study the survival of such jets at the largest scale separation to date, via 3D general relativistic magnetohydrodynamic simulations of rapidly spinning BHs immersed into uniform zero-angular-momentum gas threaded by a weak vertical magnetic field. We place the gas outside the BH sphere of influence, or the Bondi radius, chosen to be much larger than the BH gravitational radius, $R_{\rm B} = 10^3 R_{\rm g}$. The BH develops dynamically important large-scale magnetic fields, forms a magnetically arrested disk (MAD), and launches relativistic jets that propagate well outside $R_{\rm B}$ and suppress BH accretion to 1.5% of the Bondi rate, $\dot{M}_{\rm B}$. Thus, low-angular-momentum accretion in the MAD state can form large-scale jets in Fanaroff–Riley (FR) type I and II galaxies. Subsequently, the disk shrinks and exits the MAD state: barely a disk (BAD), it rapidly precesses, whips the jets around, globally destroys them, and lets 5%–10% of $\dot{M}_{\rm B}$ reach the BH. Thereafter, the disk starts rocking back and forth by angles 90°–180°: the rocking accretion disk (RAD) launches weak intermittent jets that spread their energy over a large area and suppress BH accretion to $\lesssim$2% $\dot{M}_{\rm B}$. Because the BAD and RAD states tangle up the jets and destroy them well inside $R_{\rm B}$, they are promising candidates for the more abundant, but less luminous, class of FR0 galaxies.

Unified Astronomy Thesaurus concepts: High energy astrophysics (739); Active galactic nuclei (16); Black hole physics (159); Relativistic jets (1390); General relativity (641)

Supporting material: animations

1. Introduction

Relativistic collimated outflows, known as jets, are prevalent across many astrophysical systems of vastly different scales. The largest and most energetic ones emanate from the galaxy centers that harbor supermassive black holes (SMBHs). Active galactic nuclei (AGNs), whose central SMBHs consume gas, release energy that couples to the galactic environment in a process called AGN feedback. The consensus is that the feedback comes in two flavors: (i) radio or kinetic mode, which occurs at lower accretion rates ($L \ll 0.01 L_{\rm Edd}/c^2$, where $L_{\rm Edd}$ is the Eddington luminosity)—in this mode, powerful radio jets dominate the feedback (see Fabian 2012; Morganti 2017 for reviews); and (ii) radiative or quasar mode, which takes place at high accretion rates in luminous AGNs ($L \gtrsim 0.01 L_{\rm Edd}/c^2$)—here, the radiation coupled with the surrounding gas and dust drives powerful outflows at wide angles into the galactic environment. About one in 10 luminous AGNs can produce powerful radio jets (Sikora et al. 2007). In both cases, (i) and (ii), the radio jets can propagate into the interstellar medium (ISM) and intracluster medium (ICM), displace the gas, and inflate X-ray cavities of up to several megaparsecs in size (Oei et al. 2022; see McNamara & Nulsen 2007, 2012 for reviews). Whereas these cavities appear empty in X-ray images, they are filled with relativistically hot magnetized plasma that emits copious synchrotron emission in the radio band. The cavities result from AGN feedback that can offset the runaway cooling of the ICM via shocks, acoustic waves, and/or turbulent heating and thus can regulate star formation (Zhuravleva et al. 2016; Martizzi et al. 2019; Li et al. 2020). However, how SMBHs feed on the gas, power the jets, and exert feedback on their environment remains poorly understood.

The Fanaroff–Riley (FR) classification system (Fanaroff & Riley 1974) is widely used to categorize radio galaxies into two main types, FRIs and FRIIs, determined by the morphology of their radio emission. FRIs are bright near the core and grow gradually fainter with increasing distance. FRIIs are brighter near the edge of the radio lobes and grow fainter toward the core. Recently, a new classification has been established: the FR0s that morphologically lack radio emission at scales $r \gtrsim 1$ kpc (Ghisellini 2011). They are more abundant than FRIs and FRIIs (Stecker et al. 2019), hinting that they might be

the dominant population in the local Universe (Baldi et al. 2018; see Baldi 2023 for a review). Additionally, the Fermi observatory recently detected bright γ-rays from three of $\gtrsim$100 FR0 galaxies, with two of these being an order of magnitude brighter in radio than the rest (Paliya 2021). This, along with their abundance, suggests that FR0s can significantly contribute to the isotropic γ-ray background (Stecker et al. 2019), the diffuse neutrino background (Tavecchio et al. 2018; Ackermann et al. 2022), as well as ultra-high-energy cosmic rays (Merten et al. 2021; Lundquist et al. 2022). It is not clear yet whether FR0s are part of the evolutionary stage of FRI/IIs. The SMBH mass and host environment appear similar to the FRIs, but the jet size is smaller, $r \lesssim 1$ kpc, usually unresolved, and moves slower, $\gamma \lesssim 2$ (Balmaverde & Capetti 2006; Baldi et al. 2018). This might suggest that either the BH spin or the magnetic field strength are different enough that this can affect the jet power and velocity (Baldi et al. 2018).

Spinning BHs surrounded by whirlpools of hot magnetized plasma, or accretion disks, can produce relativistic jets via the Blandford & Znajek (1977; hereafter, BZ) process. The BZ process capitalizes on the fact that as the hot plasma in the disk accretes on a spinning BH, it brings with it poloidal (pointing in the R- and z-directions) magnetic flux. BH rotation drags the inertial frames via the Lense & Thirring (1918) effect, which twists the poloidal flux in the vicinity of the BH, causing it to build up a strong toroidal component, which in turn powers collimated Poynting-flux-dominated outflows—the twin polar jets (see Tchekhovskoy 2015; Davis & Tchekhovskoy 2020). The rotation of the disk launches disk winds (via a process like that suggested by Blandford & Payne 1982) that collimate the jets into small opening angles and enable the jets to accelerate (Komissarov et al. 2009; Tchekhovskoy et al. 2009). This suggests that *rotation* is an important ingredient for accretion, jets and outflows, and their feedback on the environment. In this work, we aim to reveal the importance of ambient gas rotation on the jets and their feedback.

To understand how the jets escape out of the BH sphere of influence, one must follow them from their formation at the BH event horizon to their interaction with the ISM or ICM. For this, one needs to model the BH feeding by following the gas infall from the ISM to the BH event horizon. These are extremely arduous tasks due to the enormous scale separation of the problem. The gas originates at the edge of the BH sphere of influence, the Bondi radius (Bondi 1952):

$$R_{\rm B} = \frac{GM_{\rm BH}}{c_\infty^2} \sim 20\ {\rm pc} \times \frac{M_{\rm BH}}{10^9 M_\odot} \times \left(\frac{T_\infty}{1\ {\rm keV}}\right)^{-1}, \qquad (1)$$

which is significantly larger than the BH gravitational radius, $R_{\rm g} = GM_{\rm BH}/c^2 = 5 \times 10^{-5}\ {\rm pc} \times (M_{\rm BH}/10^9 M_\odot)$. Here, $M_{\rm BH}$ is the SMBH mass and c_∞ is the ISM sound speed. For a typical ISM temperature, $T_\infty \sim 1$ keV, the scale separation between $R_{\rm B}$ and $R_{\rm g}$ reaches 6 orders of magnitude (Russell et al. 2015, 2018). Adding to the challenge, the ICM and dark matter halos reach scales of $\sim$100 kpc, marking the scale separation of the full problem at $\sim$9–10 orders of magnitude. Dedicated galaxy simulations are capable of following gas flows from the dark matter halo down to $\sim$1 kpc scales (Anglés-Alcázar et al. 2015, 2017), and state-of-the-art hyper-refined Lagrangian simulations can even reach subparsec scales (Anglés-Alcázar et al. 2021). However, to bridge the "last mile" of the scale separation and connect the smallest scales in galaxy simulations to the event horizon, general relativistic magnetohydrodynamic (GRMHD) simulations are essential.

A popular approach for bridging the scale separation is the Bondi model (Bondi 1952; Shapiro & Teukolsky 1986), which approximates BH accretion as a spherically symmetric hydrodynamic flow. Although an elegant and simple approximation, it does not allow for jets. In this work, we add the minimum ingredients to the Bondi model that enable the study of BH-powered jet formation and propagation: we retain the zero angular momentum of the ambient gas, but add BH rotation and an ambient vertical magnetic field. We also consider the system at sufficiently high resolution and in full 3D to resolve the jet propagation and allow for the development of nonaxisymmetric instabilities in the jets.

GRMHD simulations found that magnetized accretion can accumulate large-scale poloidal magnetic fields on the BH to the point that the fields become dynamically important, i.e., able to obstruct gas infall, at which point the system enters the magnetically arrested disk (MAD) state (Bisnovatyi-Kogan & Ruzmaikin 1974, 1976; Igumenshchev et al. 2003; Narayan et al. 2003; Igumenshchev 2008) that can launch jets with energy efficiencies exceeding 100%, i.e., whose power exceeds the accretion power (Tchekhovskoy et al. 2011). In this state, the accretion continuously brings in the magnetic flux to the BH, thereby flooding both the BH and inner disk with the vertical magnetic flux. At the same time, the dynamically important magnetic flux periodically erupts from the BH, rips through the disk, and escapes. In the presence of sufficient angular momentum, the inward advection of the magnetic flux wins, and the BH is always flooded with the magnetic flux (Tchekhovskoy & McKinney 2012).

In contrast, zero-angular-momentum accretion was found to not be conducive to powerful, stable jet production. Analytic models have suggested that zero-angular-momentum accretion produces weak jets (with energy efficiency $\lesssim$1%; Das & Czerny 2012). Kwan et al. (2023; hereafter, K23) used GRMHD simulations to model the accretion of spherically symmetric magnetized gas on a rapidly spinning BH and found that zero-angular-momentum accretion could not remain in a MAD state for a prolonged period of time. The jet efficiency only transiently surpassed 100%, due to the BH eventually losing the large-scale BH magnetic flux powering the jets (see also Gottlieb et al. 2022a for a related phenomenon in collapsars) and entering the "standard and normal evolution" (SANE) state (Narayan 2012), in which the large-scale magnetic flux is subdominant and the jets are weaker or nonexistent. Ressler et al. (2021; hereafter, R21) performed 3D GRMHD simulations of spherically symmetric gas accretion onto a rapidly spinning BH ($a = 0.9375$), with a Bondi-to-event horizon scale separation of $R_{\rm B}/R_{\rm g} = 100$.[9] They varied the angle between the ambient magnetic field and BH spin directions and found that outflow efficiencies, in most cases, did not exceed 100%: the accretion flow had a hard time reaching and staying in the MAD state. Based on the results of their simulations, R21 predicted that for $R_{\rm B}/R_{\rm g} \gtrsim 800$, all jets powered by low-angular-momentum accretion will end up falling victim to the kink instability inside the Bondi radius, as is the case for realistic systems, $R_{\rm B}/R_{\rm g} \gtrsim 10^{5-6}$ (e.g., SgrA* or M87).

[9] Note that in comparison to our Equation (1), R21 use an extra factor of 2 in their Bondi radius definition: $R_{\rm B} = 2GM_{\rm BH}/c_\infty^2 = 200R_{\rm g}$.

Here, we evaluate the ability of low-angular-momentum accretion to power large-scale jets for an order-of-magnitude larger scale separation than has been possible until now. Lalakos et al. (2022; hereafter, L22) simulated a 3D GRMHD accretion of the rotating ISM for a Bondi-to-event horizon ratio of $R_{\rm B}/R_{\rm g} = 10^3$. Here, we follow the L22 approach, but consider zero-angular-momentum accretion. As in L22, we include a rapidly spinning BH, $a = 0.94$, and a large-scale vertical magnetic field, which is aligned with the BH spin vector. To study the self-consistent jet formation and propagation to distances well outside the Bondi radius, we use adaptive mesh refinement (AMR) to ensure sufficient resolution of the tightly collimated jets.

More generally, we aim to understand the basic ingredients necessary for the formation of stable jets or, conversely, what it takes to "break" them. Namely, we aim to answer questions such as: is gas angular momentum (and the formation of an accretion disk) needed to maintain jet stability? Is there a critical power above which the jets manage to escape the BH sphere of influence? How does the ambient medium trigger jet instability? What are the observational signatures of unstable jets and how do they fit within the FR morphological classification?

Throughout the paper, we work in units of $G = M = c = 1$. For conciseness, we sometimes measure the time in the unit of $1000R_{\rm g}/c$, which we denote as 1k: e.g., $7.5 \times 10^4 R_{\rm g}/c \equiv 75$ k. In Section 2, we describe our simulation setup and choice of the initial physical parameters. In Section 3, we present the properties of the accretion flow and jets as measured near the BH. In Section 4, we show how the jets can escape out of the Bondi sphere and discuss their stability. In Section 5, we show how changes in the behavior of accretion flow angular momentum can lead to the destruction of the jets. In Section 6, we compare internal and external kink instabilities. Finally, in Section 7, we summarize and discuss our results.

2. Numerical Method and Setup

We carry out our simulations using the GRMHD code H-AMR, which includes advanced features such as graphics processing unit acceleration, AMR, and local adaptive time-stepping (Liska et al. 2022). We initialize the simulation by placing a BH inside a uniform static ambient medium. We consider a rapidly spinning BH, with dimensionless spin $a = 0.94$, to favor jet launching. To allow the system to evolve naturally, we avoid prescribing the conditions inside $R_{\rm B}$: we carve out a cavity inside the Bondi sphere ($r < R_{\rm B}$) and place the ambient gas of uniform rest-mass (RM) density, $\rho = \rho_\infty$, outside the sphere ($r \geqslant R_{\rm B}$).

We choose the ambient sound speed, c_∞, to achieve the desired scale separation, $R_{\rm B} = 10^3 R_{\rm g}$ (Equation (1)). This is similar to L22, but here we set the ambient medium angular momentum to zero. In this work, we focus on low-luminosity BH accretion systems. Because of this, we do not include any radiation effects (e.g., radiative cooling), which are important at higher-mass accretion rates. Thus, our simulations are nonradiative and scale-free: the simulation results trivially rescale to any value of ρ_∞. As appropriate for AGN environments at the Bondi radius, we adopt a monatomic nonrelativistic ($\Gamma = 5/3$) gas with an ideal gas equation of state, $p_{\rm g} = (\Gamma - 1)u_{\rm g}$, where $p_{\rm g}$ and $u_{\rm g}$ are the pressure and internal energy density of the gas.

Outside the Bondi radius, we include a large-scale vertical magnetic field in the direction parallel to the BH spin. Asymptotically far away, we set $\boldsymbol{B} = B_0 \boldsymbol{a}$. Closer to $R_{\rm B}$, we deform the field such that the radial component of the magnetic field, B^r, smoothly vanishes toward the edge of the cavity and no field enters the cavity, $r \leqslant R_{\rm B}$. To achieve this, we adopt the magnetic vector potential, $A_\varphi \propto \max[(r^2 - R_{\rm B}^2), 0]\sin^2\theta$. We normalize the strength of the magnetic field such that the thermal-to-magnetic pressure ratio is $\beta = p_{\rm g}/p_{\rm m} = 100$ asymptotically far away (this also ensures that $\beta \geqslant 100$ everywhere). Here, $p_{\rm m} = b^2/8\pi$ is the magnetic pressure, where $b^2 = b^\mu b_\mu$ and b^μ is the comoving contravariant magnetic field four-vector (defined in Appendix A). In order to break axisymmetry and provide the seeds for the growth of the magneto-rotational instability (MRI; Balbus & Hawley 1991), we include random pressure perturbations at a 2% level in the initial conditions.

We note that the cavity is, technically, not entirely empty, because GRMHD codes cannot handle vacuum. To prevent ρ and u_g from becoming extremely low or negative in highly magnetized regions (i.e., the jet launching regions), our numerical scheme adopts the following density floors. If at any point in the simulation the densities drop below the floor values, $\rho < \rho_{\rm fl} = \max[b^2/(60\pi), 10^{-7}r^{-2}, 10^{-20}]$ and/or $u_{\rm g} < u_{\rm g,\,fl} = \max[b^2/(3000\pi), 10^{-9}r^{-2\Gamma}, 10^{-20}]$, then we add mass and/or internal energy, respectively, in the drift frame until the floor values are reached (see Appendix B3 of Ressler et al. 2017).

We construct our grid in spherical polar coordinates, r, θ, and φ. The radial grid is uniform in $\log r$, and r spans $0.83R_{\rm H} \leqslant r \leqslant 10^6 R_{\rm g}$. There are six cells inside the event horizon, $R_{\rm H} = R_{\rm g}(1 + \sqrt{1 - a^2})$, and the radius of the outer boundary is larger than the light travel distance in a simulation duration: these ensure that both the inner and outer radial boundaries are causally disconnected from and cannot influence the solution. The polar and azimuthal grids are uniform in the θ- and φ-directions and span $0 \leqslant \theta \leqslant \pi$ and $0 \leqslant \varphi \leqslant 2\pi$, respectively. We use outflow, transmissive, and periodic boundary conditions in the radial, polar, and azimuthal directions, respectively (Liska et al. 2022). The base grid resolution is $N_r \times N_\theta \times N_\varphi = 448 \times 96 \times 192$ cells in the r-, θ-, and φ-directions. At $r \geqslant 6.5R_{\rm g}$, we activate one level of static mesh refinement (SMR): this doubles the resolution in each dimension, leading to an increased effective resolution of $896 \times 192 \times 384$. On top of the SMR, we also include two additional AMR levels that we dynamically activate during the run, to ensure sufficient resolution to resolve the collimated jets and cocoons at large radii, as we describe in Appendix B. The maximum effective resolution in the jets can therefore reach $3584 \times 768 \times 1536$ cells.

In order to avoid the polar singularity interfering with highly magnetized jet regions, we tilt the entire BH–gas system by 90° relative to our computational grid: as a result, the BH rotational axis is perpendicular to the polar singularity of our computational grid. However, for the sake of narrative simplicity, we present our results below as if we did not perform the tilt: for presentation purposes, we direct the z-axis along the BH spin vector and count off the polar angle, θ, from the BH spin direction.

3. MAD Prologue

The simulation starts with the constant-density ambient gas at rest, located outside of the empty cavity, $r \geqslant R_{\rm B}$ (Section 2).

The pressure gradient at the edge of the cavity, along with the gravitational attraction from the BH, push the gas inward. To study the mass flow in our simulation, we define the RM component of the energy flux density:

$$f_{\rm RM} = \rho c^2 u^r, \tag{2}$$

whose surface integral gives us the net energy outflow rate or power:

$$\dot{E}_{\rm RM} = \iint f_{\rm RM}\, dA, \tag{3}$$

where $dA = \sqrt{-g}\, d\theta d\varphi$ is the differential surface element, $g = |g_{\mu\nu}|$ is the determinant of the metric, and u^μ is the coordinate-frame contravariant proper velocity vector. In a steady state, $\dot{E}_{\rm RM}$ is conserved and independent of radius. We evaluate the BH mass accretion rate as the negative of the RM power, $\dot{M} \equiv -\dot{E}_{\rm RM}(r = 8R_{\rm g})/c^2$, which we measure at $r = 8R_{\rm g}$ to avoid potential contamination by the density floors near the event horizon.

Figure 1(a) shows the time dependence of $\dot{M}$, which peaks at approximately the analytic Bondi prediction,

$$\dot{M}_{\rm B} = 4\pi\lambda_{\rm s}(GM_{\rm BH})^2 \frac{\rho_\infty}{c_\infty^3}, \tag{4}$$

at about a freefall time $t_{\rm ff} = 2^{-1/2}(R_{\rm B}/R_{\rm g})^{3/2} R_{\rm g}/c \simeq 2.2 \times 10^4 R_{\rm g}/c = 22$ k after the beginning of the simulation. Here, for our choice, $\Gamma = 5/3$, we have $\lambda_{\rm s} = 1/4$ (Shapiro et al. 1976; Di Matteo et al. 2003). That $\dot{M}$ reaches the simple analytic Bondi prediction, $\dot{M}_{\rm B}$, is not entirely surprising, because, in the absence of any external angular momentum supply, the gas never encounters a centrifugal barrier, which would inhibit the accretion relative to the Bondi expectation.

The infalling gas drags inward the large-scale vertical magnetic flux, and some of it makes it all the way to the event horizon, resulting in the increase of the absolute BH magnetic flux:

$$\Phi_{\rm BH} = 0.5 \iint |B^r|\, dA. \tag{5}$$

Here, the integral is over the entire event horizon of the BH, and the factor of 0.5 converts it to a single hemisphere. Figure 1(b) shows the time dependence of the normalized absolute magnetic flux:

$$\phi_{\rm BH} = \frac{\Phi_{\rm BH}}{\sqrt{\langle \dot{M} \rangle_\tau R_{\rm g}^2 c}}, \tag{6}$$

which measures the strength of the magnetic flux relative to the onslaught of the infalling gas; here, to clarify the units, we explicitly include the length and velocity scaling factors, and $\langle \dot{M} \rangle_\tau$ is the rolling average of the mass accretion rate over the time interval of $\tau = 3$ k. This time interval is sufficiently long to average over the strong $\dot{M}$ oscillations in the MAD state. We also consider a signed magnetic flux through the northern hemisphere,

$$\Phi_{\rm N} = \int_0^{\pi/2} d\theta \int_0^{2\pi} d\varphi B^r \sqrt{-g}\,, \tag{7}$$

as well as its normalized form, $\phi_{\rm N}$, defined analogous to Equation (6). As the infalling gas continuously drags more of the ambient magnetic flux inward, the BH magnetic flux grows in strength and $\phi_{\rm BH}$ steadily increases.

Similar to Equation (3), we compute the various components of the energy flux using the stress–energy tensor:

$$T^\kappa_\lambda = \left(\rho c^2 + u_{\rm g} + p_{\rm g} + \frac{b^2}{4\pi}\right) u^\kappa u_\lambda + \left(p_{\rm g} + \frac{b^2}{8\pi}\right)\delta^\kappa_\lambda - \frac{b^\kappa b_\lambda}{4\pi}. \tag{8}$$

We are interested in the radial energy flux and set $\kappa = r$ and $\lambda = t$. Thus evaluated, Equation (8) gives us the total radial energy flux, $f_{\rm TOT}$. The electromagnetic (EM), thermal (TH), and kinetic energy (KE) flux density components of the total energy flux, respectively, are:

$$f_{\rm EM} = -(b^2 u^r u_t - b^r b_t)/4\pi, \tag{9}$$

$$f_{\rm TH} = -(u_{\rm g} + p_{\rm g}) u^r u_t, \tag{10}$$

$$f_{\rm KE} = -\rho c^2 u^r u_t, \tag{11}$$

where u^r is the radial contravariant four-velocity component and u_t is the temporal covariant velocity component, which is a conserved quantity for point masses. We also define the components of power (integral versions of the flux densities), Equations (9)–(11), following Equation (3):

$$\dot{E}_\# \equiv \iint f_\# \, dA, \tag{12}$$

where # = EM, TH, KE, or RM. The integral version of Equation (9) gives us the jet power, $L_{\rm j} = \dot{E}_{\rm EM}(r = 8R_{\rm g})$, which we measure through a sphere of radius $r = 8R_{\rm g}$. Note that $L_{\rm j}$ includes the power of both jets. Figure 1(c) shows that $L_{\rm j}$ abruptly increases at $t \simeq 24$ k once $\phi_{\rm BH}$ exceeds a critical value, $\phi_{\rm BH} \simeq 15$, and the jets form.

Figure 1(d) shows the outflow energy efficiency, $\eta \equiv L_{\rm j}/\langle \dot{M} c^2 \rangle_\tau$, which is the jet power measured in units of BH accretion power: at $t \simeq 24$ k, it is not yet very high, but it is still significant, $\eta = 0.1 \equiv 10\%$—from now on, we will express all fractions in terms of percent. Although at this time the jets have not yet reached the maximum efficiency, they already exert significant feedback on the accretion flow and suppress the BH accretion rate relative to its peak by nearly an order of magnitude, $\dot{M}/\dot{M}_{\rm B} \sim 20\%$, via injecting the energy into the accretion flow and partially unbinding it. This marks the end of the initial transient phase, during which the system settles into a quasi-steady state.

Figure 1(b) shows that the dimensionless BH magnetic flux grows until it saturates around $\phi_{\rm BH} \gtrsim 50$ at $t \gtrsim 31$ k. At this time, the BH magnetic flux becomes dynamically important, i.e., the magnetic pressure can withstand the onslaught of the total momentum flux of the infalling gas. This signals the formation of a MAD (Tchekhovskoy et al. 2011). The jets produced during the MAD state attain the maximum power for a given $\dot{M}$, increasing their chance of reaching the Bondi scale and producing feedback. This suppresses the mass accretion rate to $\langle \dot{M} \rangle/\dot{M}_{\rm B} = 1.5\%$, a staggering reduction by nearly 2 orders of magnitude from the peak, and the analytical Bondi (1952) expectation, $\dot{M}_{\rm B}$. The average jet power, $\langle L_{\rm j} \rangle/\dot{M}_{\rm B} c^2 \simeq 2.9\%$, translates into extremely high jet efficiency, $\langle \eta \rangle \simeq 190\%$: this implies that the BH energy output in the form of jets exceeds the energy input in the form of the RM energy. This is typical for rapidly spinning ($a \geqslant 0.9$) MAD

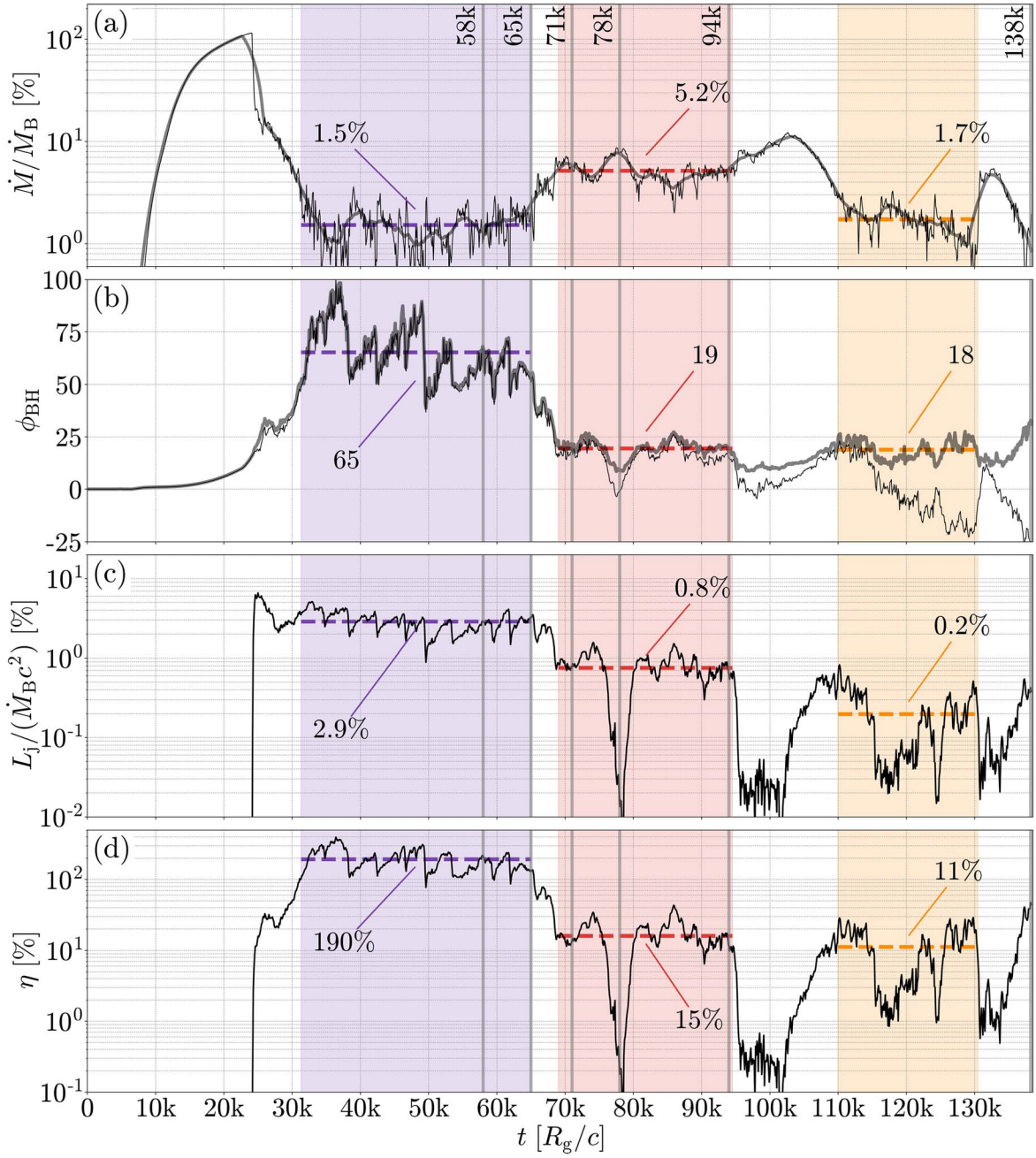

Figure 1. In the absence of rotation and a strong magnetic field, the instantaneous BH mass accretion rate can transiently reach the Bondi value, $\dot{M} \simeq \dot{M}_{\rm B}$ (the thin line in panel (a)). However, once the magnetic flux accumulates on the BH event horizon and its normalized absolute value exceeds $\phi_{\rm BH} \approx 15$ at $t = 24$ k (the thick line in panel (b)), the first jets—of normalized power $L_{\rm j}/\dot{M}_{\rm B}c^2 \simeq 5\%$ (panel (c)) and efficiency $\eta \simeq 10\%$ (panel (d))—emerge and suppress the instantaneous BH accretion rate to $\dot{M}/\dot{M}_{\rm B} \simeq 20\%$ (the thin line in panel (a); we normalize $\phi_{\rm BH}$ and η to $\langle\dot{M}\rangle_\tau$, which is $\dot{M}$ smoothed over $\tau = 3$k and shown with the thick line in panel (a)). Following this initial transient phase, the accumulating magnetic flux reaches $\phi_{\rm BH} \gtrsim 50$ (the thick line in panel (b)) and leads to a MAD state (the purple shaded region; 31 k $\leqslant t \leqslant$ 65 k). In a MAD state, jets of high power, $\langle L_{\rm j}\rangle/\dot{M}_{\rm B}c^2 \simeq 2.9\%$ (panel (c)) and efficiency, $\langle\eta\rangle \simeq 190\%$ (panel (d)), severely suppress BH accretion to $\langle\dot{M}\rangle/\dot{M}_{\rm B} \simeq 1.5\%$ (panel (a); Section 3). At $t \gtrsim 65$ k, the system exits the MAD state, the jets become weaker, $\langle\eta\rangle \lesssim 15\%$, and the mass accretion rate higher, $\langle\dot{M}\rangle/\dot{M}_{\rm B} \lesssim 5\%$ (the red shaded region; 69 k $\leqslant t \leqslant$ 95 k). The jets sometimes completely shut off and fall apart (e.g., at $t = 78$ k and 96–102 k; Section 4) when the normalized northern hemisphere BH magnetic flux vanishes, $\phi_{\rm N} = 0$ (the thin line in panel (b)), η drops (to $\lesssim$0.1%; panel (d)), and the reduced jet feedback allows higher $\dot{M}/\dot{M}_{\rm B} \lesssim 10\%$ (panel (a)). However, even such weaker jets can suppress $\dot{M}$ similar to the MAD state, $\langle\dot{M}\rangle/\dot{M}_{\rm B} \simeq 1.7\%$, for extended periods of time if they continuously reorient (the orange shaded region; 110 k $\leqslant t \leqslant$ 130 k; Section 5 and Figure 4). In all panels, the horizontal dashed lines show time average values, which are also labeled with callouts.

BHs, whose rotational energy is extracted—by the continuous winding of magnetic fields on the event horizon—faster than the accretion can replenish it (Tchekhovskoy et al. 2011; McKinney et al. 2012; Tchekhovskoy & McKinney 2012). Figure 1(b) shows that at $t \gtrsim 65$k, the normalized magnetic flux drops below the characteristic MAD value, $\phi_{\rm BH} = 50$, the flow exits the MAD state, and the jets become progressively weaker (Figure 1(c)) until their complete destruction at the event horizon at $t = 78$ k, when $\eta \leqslant 0.1\%$ (Figure 1(d)). With no strong jets to obstruct the accretion, the mass accretion rate (Figure 1(a)) increases from $\dot{M}/\dot{M}_{\rm B} \sim 1.5\%$ in the MAD state to $\dot{M}/\dot{M}_{\rm B} \lesssim 10\%$ in the SANE state.

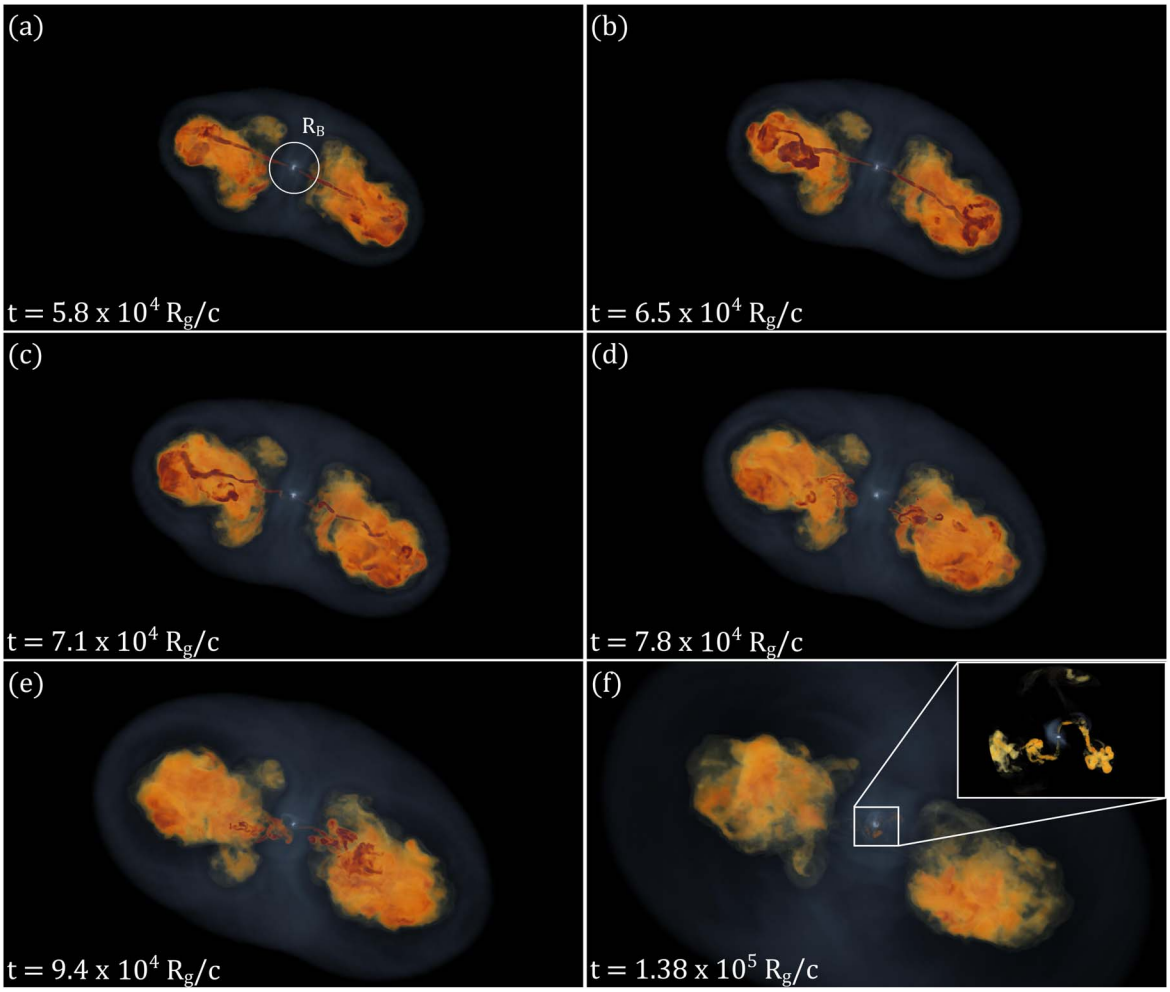

Figure 2. 3D volume renderings of density at different times show that as jets propagate out of the Bondi sphere, they become kink-unstable and globally fall apart. The BH spin is pointing in the direction of jet propagation to the right in panel (a). An animation is available and on YouTube. The animation runs from $t = 0$ to $t = 1.4 \times 10^5 R_g/c$. The real-time duration of the animation is 14 s. (a) The highly powered MAD jets (red) easily escape the Bondi sphere without obvious signs of instability, except near the head. At the contact points (hotspots), at which the jets drill through the ambient gas, the shocked jet material spills sideways, creates backflows, and forms the cocoons (yellow). The relativistic motion of the jets and cocoons shocks the ambient gas via bow shocks (blue). (b) As the jets propagate farther out, this leaves enough time for the kink instability to grow, and it leads to helical bends near the hotspot. (c) The jet power decreases by ∼4, and the kink-unstable regions move in closer to the BH. The decrease in power propagates through the jets faster than the cocoons can react, and the weakened jets get squeezed by the cocoons. (d) The central engine shuts off, and the jets break apart globally. (e) Weakened jets wobble and lose focus: without consistent energy supply from the jets, mildly magnetized cocoons become relics, which buoyantly rise outward. Meanwhile, the wobbling jets transiently form and fall apart, without an opportunity to reach the Bondi sphere. (f) Intermittent and weaker jets form, but get deflected sideways, as the accretion disk tilt continuously changes. The inset image shows that the jets develop extreme bends inside the Bondi radius.

(An animation of this figure is available.)

4. A Twisted Interlude

In this section, we explore the large-scale stability and propagation of the jets, and how they reach and impact the BH feeding scales at $r \gtrsim R_B$. Some jets can traverse vast distances, sometimes larger than the galaxy itself (e.g., Cygnus A; Perley et al. 1984), whereas others appear to perish within the galaxy (e.g., M87; Biretta et al. 1991). This involves a scale separation of ∼10 orders of magnitude from the BH to the outskirts of the galaxy. Along the way, the jets survive in the face of many obstacles, each of which can become a major dissipation-triggering event (e.g., internal, external, and/or recollimation shocks, MHD instabilities, magnetic reconnection, etc.), where a significant fraction of the jet energy can transform into radiation, and the jet can become locally or globally disrupted. Indeed, magnetized jets are prone to current-driven instabilities, with the kink instability being perhaps the most destructive (Bateman 1978; Lyubarskij 1992; Begelman 1998; Lyubarskii 1999; Eichler 1993; Narayan et al. 2009). The kink instability acts on the jet core, dislodging it from its original location and twisting it into a helical structure. In ambient media with a flat density profile, $\rho \propto r^{-\alpha}$, where $\alpha < 2$, the kink instability is inevitable (Bromberg & Tchekhovskoy 2016; hereafter, BT16): in such a medium, a jet with a constant opening angle would displace progressively more and more gas as it propagates out. The jet responds by becoming progressively more collimated. As we will see below (Section 4.1), this makes it more susceptible to the kink instability that can cause the jets to fall apart.

To visualize the large-scale morphology and evolution of the jets, we have created a 3D volume-rendered animation. We present a sequence of key snapshots in Figure 2, taken at the times indicated by the vertical lines in Figure 1. The jets are launched at $t = 24$ k (Figure 1(c)), and by $t \simeq 28$k they reach the Bondi sphere and start interacting with the ambient medium

(not shown in Figure 2). Figure 2(a) shows that by $t = 58$ k, the high-power MAD jets (red) drill their way through the ambient medium out to $r \simeq 4000R_g = 4R_B$. As the jets ram into the ambient medium, they form strong twin bow shocks at the jet heads. The shocks increase the internal energy at the heads, which typically renders these regions observable as hotspots. At the head, jet material spills sideways and flows back to create the *inner cocoon* (orange), and the strong bow shock, caused by the jet's relativistic motion, heats up the ambient gas to create the *outer cocoon* (blue). The jets are mostly straight, apart from the bends in the outer half of the jets ($r \gtrsim 2000R_g$). Figure 2(b) shows that at later times, $t = 65$ k, these bends become more pronounced, e.g., one of them twists the jet into a knot, as seen at $r \simeq 2000R_g$ in the left jet.

Soon after this, the MAD state comes to an end: by $t = 71$k, the jet power drops by a factor of ~4 (Figure 1(c)). Figure 2(c) shows that the jets become more helical: the kink instability affects a larger fraction of the jet length, with the first jet bend showing up already at $r \lesssim 1000R_g$. Figure 2(d) reveals that by $t = 78$ k, the jets get globally destroyed: at this time, the power of the jets essentially vanishes (Figure 1(c)) and they no longer focus their energy into the twin cocoons. At later times, Figures 2(e)–(f) show that short-lived jets still form close to the BH, but fall apart around, or even inside, the Bondi radius, and starve the cocoons of energy. With the energy supply via the jets mostly shut off, the mildly magnetized cocoons become relics, with a combination of leftover momentum and buoyancy, and occasional mergers with smaller cavities inflated by the wobbling jets, driving them outward. At large scales, although weakened, bow shocks are still present and outrun the cocoons, while injecting energy and momentum into the ambient gas.

4.1. Jet Stability Criterion

To quantitatively analyze the development of the kink mode in the jets, we use Equations (3) and (9)–(11) to express the ratio of total to RM energy fluxes:

$$\mu \equiv \frac{f_{\rm TOT}}{f_{\rm RM}} = -u_t(1 + h + \sigma), \tag{13}$$

which gives the maximum Lorentz factor a fluid element attains if all of its EM and thermal energy fluxes are converted into the KE flux. To obtain Equation (13), we used the facts that $f_{\rm TOT} = f_{\rm KE} + f_{\rm TH} + f_{\rm EM}$ and

$$-u_t = \frac{f_{\rm KE}}{f_{\rm RM}} \approx \gamma, \tag{14}$$

and introduced the relativistic gas enthalpy per unit mass,

$$w \equiv \frac{f_{\rm KE} + f_{\rm TH}}{f_{\rm KE}} = 1 + \frac{u_g + p_g}{\rho c^2} = 1 + h, \tag{15}$$

where h is the nonrelativistic gas enthalpy per unit mass (i.e., without the RM contribution), and magnetization:

$$\sigma \equiv \frac{f_{\rm EM}}{f_{\rm KE}} \approx \frac{b^2}{4\pi\rho c^2}, \tag{16}$$

where the approximate equalities in Equations (14) and (16)[10] are accurate at large distances from the BH (Chatterjee et al. 2019). Below, unless stated otherwise, we will use the right-hand sides of Equations (13), (15), and (16) as expressions for μ, h, and σ, respectively.

The jets consist of an inner core of cylindrical radius, R_c, dominated by the poloidal comoving magnetic field component, b_p, and an outer region, dominated by the toroidal comoving field component, $b_{\rm tor}$ (BT16). Here, $R_c = r\sin\theta_c$ corresponds to the opening angle of the jet core, θ_c, at distance r, and we measure both b_p and $b_{\rm tor}$ in the fluid frame (see Appendix A). The kink instability growth timescale for a local fluid element is approximately the time it takes for an Alfvén wave to travel around the circumference of the jet at the Alfvén velocity:

$$v_A = c\sqrt{\frac{\sigma}{1 + h + \sigma}}. \tag{17}$$

We define the kink instability growth timescale, as measured in the lab frame:

$$t_{\rm kink} \equiv \eta_{\rm kink}\frac{2\pi R\gamma}{v_A} \times \frac{b_p}{b_{\rm tor}} \simeq \eta_{\rm kink}\frac{2\pi R_c\gamma}{v_A}, \tag{18}$$

where we used the jet Lorentz factor, γ, to convert the timescale from the fluid frame to the lab frame. The ratio, $b_p/b_{\rm tor}$, is the magnetic winding, and $R \times b_p/b_{\rm tor}$ is the pitch, where $R = r\sin\theta$ is the cylindrical radius of the jet location in question. The factor, $\eta_{\rm kink} \simeq 5$–10, is the poorly constrained prefactor that enters the kink timescale for the jet to become considerably deformed (Mizuno et al. 2009, 2012; Bromberg et al. 2019). The approximate equality in Equation (18) evaluates the timescale at the edge of the jet core, where, by definition, $b_p = b_{\rm tor}$, and the value of the pitch is simply R_c. The kink instability develops in the fluid frame, and the available time for its growth is the propagation time of the jet fluid from the BH, moving at velocity v. In the lab frame, this dynamical time is:

$$t_{\rm dyn} = \int_0^r \frac{dr'}{v} \simeq \frac{r}{v}, \tag{19}$$

where we assume constant jet velocity, v, ignoring the initial acceleration of the jet, and assume that the jet travels only in the radial direction (not true in a bent jet). The ratio of the kink to the dynamical timescale (Equations (18) and (19)) gives the jet stability parameter:

$$\Lambda = \eta_{\rm kink}\frac{2\pi R_c\gamma v}{v_A r}. \tag{20}$$

The jet is stable at $\Lambda > 2$ and unstable at $\Lambda < 2$ (BT16). Calculating the radius of the jet core is a nontrivial task, since the jet core can displace itself from the z-axis in a nonaxisymmetric fashion. To compute R_c, we first evaluate the solid angle subtended by the jet core, Ω_c, which we identify as satisfying both the $\mu > 3$ and $b_p \geqslant b_{\rm tor}$ conditions. We then calculate the core opening angle using $\Omega_c = 2\pi(1 - \cos\theta_c)$ and obtain its cylindrical radius, $R_c = r\sin\theta_c$. Without loss of generality, we focus on one of the twin jets, the one pointing in the direction of the BH spin, $\vec{a}$.

[10] We ignore the term $b^r b_t$ in the approximate equality in (16), since $b_t \approx -b^r = -B^i u_i \approx 0$ asymptotically far from the BH ($r \gtrsim 10R_g$) outside of current sheets (see Appendix A).

4.2. Jet Bends Set the Speed Limit

Figure 3(a1) shows a transverse projection of the jet proper velocity, γv, at $t = 58$ k (the same time as in Figure 2(a)). Here, we average γv along the line of sight (which is perpendicular to the direction of BH spin, $\vec{a}$), and weigh it with the magnetization, σ, to highlight the internal structure of the jet. At this time, most of the jet is free of significant bends, except toward the head, at $r \gtrsim 2000R_g = 2R_B$. As the jet bends, its proper velocity drops from $\gamma v \simeq 3$ (dark blue) to $\gamma v \simeq 1.7$ (green), which corresponds to $\gamma \simeq 2$: the slower the jet, the easier for it to make sharp turns. The jet maintains its transrelativistic proper velocity until it reaches the head (hotspot), splashes sideways and backward, and creates the backflows (brown) at $\gamma v \lesssim 1$. Figure 3(a2) shows the jet after the MAD state has ended, at $t = 71$ k (the same time as in Figure 2(c)). By this time, the average jet power has decreased by a factor of ∼4, compared to Figure 3(a1). Weaker jets are less rigid, thus their interaction with the ambient medium can bend them more easily. Indeed, the jet develops bends that are much stronger and closer to the BH than in the MAD state. These bends force most of the jet to become mildly relativistic, $\gamma v \leqslant 1.7$. Even tiny, visually imperceptible, bends can have dramatic consequences for relativistic jets.

For relativistically magnetized jets, the consequences can become particularly dire when the jets become superfast magnetosonic, i.e., when they outrun their own fast magnetosonic waves, which for cold flows translates to a proper velocity $u_F = \gamma_F v_F \approx \sigma^{1/2}$ (Tchekhovskoy et al. 2010). If we introduce the fast Mach number, $M_F = \gamma v / u_F \approx \gamma v / \sigma^{1/2}$, we can write the fast-wave Mach cone opening angle as

$$\theta_{\rm Mach} \equiv \sin^{-1}\frac{1}{M_F} \approx \frac{u_F}{\gamma v} \approx \frac{\sigma^{1/2}}{\gamma v}, \tag{21}$$

where the first approximate equality applies when the jets are in the highly superfast magnetosonic regime, $M_F \gg 1$ and the latter applies in the cold limit. Why do relativistic jets have a hard time making turns? This is because in order for a jet to navigate a turn smoothly, the jet must be able to anticipate that the turn is coming. Here, $\theta_{\rm Mach}$ gives the jet's "field-of-vision" angle, i.e., the maximum angular deviation within which fast waves can mediate the total pressure perturbations. Thus, the jets cannot bend by more than the fast Mach cone opening angle,

$$\theta_{\rm bend} \lesssim \theta_{\rm Mach} \approx \frac{u_F}{\gamma v} \approx \frac{\sigma^{1/2}}{\gamma v}; \tag{22}$$

or, equivalently, the jets cannot exceed the "speed limit," $u_{\rm max}$:

$$\gamma v \lesssim u_{\rm max} \equiv \frac{u_F}{\theta_{\rm bend}} \approx \frac{\sigma^{1/2}}{\theta_{\rm bend}}, \tag{23}$$

where the latter approximate equality applies in the cold limit. The stronger the bend (larger $\theta_{\rm bend}$), the smaller the speed limit, $u_{\rm max}$, which is the maximum allowed jet proper velocity, γv, for which the jets avoid the development of internal shocks. If γv exceeds $u_{\rm max}$, the jets develop oblique internal shocks that discontinuously reduce the jet velocity. Bends are not the only mechanism through which jets can develop shocks and decelerate. For instance, if the jets conically expand into a medium, they accelerate rapidly and soon become superfast magnetosonic. At some point, the pressure of the hot cocoons engulfing the jets starts to dominate over the jet internal pressure and squeezes the jets. As a result, the jets develop collimation shocks behind which the jet material slows down. Magnetic stresses operating downstream of the shocks introduce additional compression forces that cause the jets to pinch and form narrow nozzles in which the kink instability can grow more efficiently and dissipate energy (e.g., Lyubarsky 2009; BT16; Barniol Duran et al. 2017).

4.3. What Triggers Kink Instability in Our Jets?

Figure 3(b) shows the radial profiles of proper, γv (magenta), and Alvén, v_A (green), velocities, which we have angle-averaged over the jet core of radius R_c (shown in gold; see Section 4.1 for a definition). For comparison, we also show the radius of the jet, R_j (dark red). Using Equation (20), we can now compute the stability parameter, Λ (blue): here, the line thickness indicates the uncertainty range of $\eta_{\rm kink} = 5$–10 in the definition of the stability parameter. That $\Lambda \gtrsim 2$ at $r \lesssim 1500R_g$ in Figure 3(b1) implies that according to the stability criterion, the jet is expected to be stable: Figure 3(a1) shows that at these distances, the jet appears to be mostly straight. At larger radii, however, we have $\Lambda \lesssim 2$, suggesting an instability: consistent with this expectation, the jet develops bends at $r \gtrsim 1500R_g$. At the later time, Figure 3(b2) shows that $\Lambda \lesssim 2$ throughout most of the jet, already at $r \gtrsim 500R_g$, indicating that according to the stability criterion, we expect that most of the jet is susceptible to the kink instability. Figure 3(a2) shows multiple strong bends throughout the lengths of the jet. We note that strictly speaking, Equation (20) is only valid for small perturbations (i.e., in the limit of small jet bends) and is not applicable once the bends become extreme (see Section 6).

Figure 3(b1) shows that in the stable region, at $r \lesssim 1500R_g$, the jet core is relativistic, $\gamma v \simeq 3$, with an average radius of $R_c \simeq 20R_g$. The multiple dips in γv correspond to recollimation or oblique shocks in the jet, at $r/R_g \simeq 800$, 1300, and 1500. At these locations, the velocity drops to $\gamma v \simeq 2$, while the jet and core radii dip; Figure 3(a1) shows that the jet tends to develop bends at the same locations. At $r \gtrsim 2000R_g$, the jet displays its largest bend: at the beginning of the bend, the jet velocity dips to $\gamma v \simeq 1.5$ and the core radius dips to $R_c \lesssim 10R_g$. As the jet bend proceeds, the core radius gradually increases to $R_c = 50R_g$, likely reflecting the dissipation of the toroidal field; the velocity also recovers and levels off at $\gamma v \gtrsim 2$. Neither the jet radius R_j, which remains ∼3–4 times wider than the core, nor the Alfvén speed, which remains roughly constant at $v_A/c \sim 0.5$–0.7, appear to be affected by the bend.

At the later time, Figure 3(b2) shows that the jet core moves at a transrelativistic speed, $\gamma v \lesssim 2$, and both R_c and Λ show multiple dips, likely associated with oblique shocks (e.g., at $r/R_g \simeq 400$ and 600), at which the stability parameter dips down to an unstable level, $\Lambda < 2$, indicating the presence of the instability. Figure 3(a2) shows that the jet disrupts at $r = 800R_g$ and the velocity decreases to $\gamma v \lesssim 1$. At the same time, both R_c and R_j spike due to the $r =$ constant cross section slicing the jets at an angle and making jet features appear wider. Even at such high resolutions as ours, the simulation resolves the transverse extent of the jet core (∼$30R_g$) out to $r \simeq 1500R_g$ by five cells. The simulation resolves the transverse extent of the jet (∼$100R_g$) out to $r \simeq 5000R_g$ by five cells, although at such

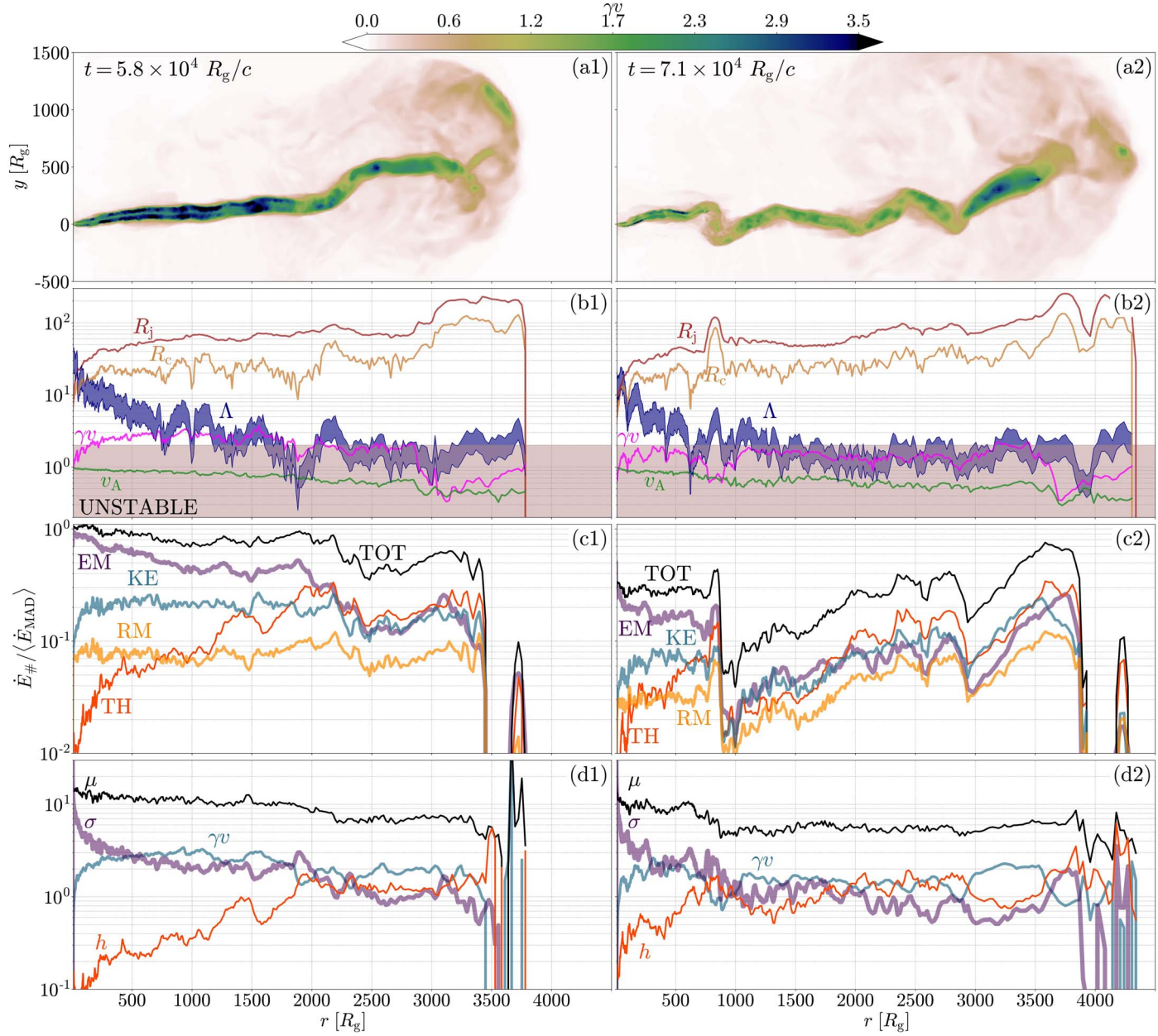

Figure 3. The kink instability disrupts the jets as their power drops fourfold upon the exit out of the MAD state at $t \approx 65$ k. (a) Transverse projection of σ-weighted proper velocity, γv, reveals large-scale jet bends, telltale signs of the kink instability. (b) Whereas at the earlier time ($t = 58$ k; panels (a1) and (b1)), only the outer jet, $r \gtrsim 2000 R_g$, shows bends and satisfies the kink instability criterion, $\Lambda \lesssim 2$, at the later time ($t = 71$ k; panels (a2) and (b2)), most of the jet, $r \gtrsim 800 R_g$, shows bends and satisfies the criterion. The jet bends cause the core average proper jet velocity γv (magenta) to significantly decrease from $\gamma v \simeq 3$ (panel (b1)) to $\gamma v \lesssim 2$ (panel (b2)) and result in a comparable decrease in Λ (Equation (20)). Although the jet radius, R_j (dark red), also decreases, this noticeably affects neither the core radius, R_c (gold), nor the core average Alfvén velocity, v_A (green). (c) Surface-integrated fluxes, or power, through the jet ($\mu > 3$) normalized to the time average total MAD power, $\langle \dot{E}_{MAD} \rangle$. The normalized total jet power, $\dot{E}_{TOT}$ (black), remains approximately constant in stable jet regions. The KE component, $\dot{E}_{KE}$ (light blue), gradually increases at the expense of the EM component, $\dot{E}_{EM}$ (purple), which dominates the total energy power until the instability sets in at $r \gtrsim 2000 R_g$ in panel (c1) and $r \gtrsim 800 R_g$ in panel (c2). Panels (a1) and (a2) show that in the unstable regions, the jet develops one or more bends. Whereas just before each substantial bend, the thermal component (orange–red) grows up to equipartition with the EM component (purple), $\dot{E}_{TH} \sim \dot{E}_{EM}$, after each bend, all the power components drop, followed by a gradual increase until the next bend (e.g., for the bends at $r/R_g \simeq 800$, 1300, 2000, 2500, and 3000 in panel (c2)): we attribute this to the "accordion" effect—the jet bends allow the jets to elongate and rarefy longitudinally. The RM power $\dot{E}_{RM}$ (orange) remains subdominant to the rest of the components. (d) The jet average proper velocity, γv (light blue; obtained via $\gamma \equiv \dot{E}_{KE}/\dot{E}_{RM}$), increases as the jets accelerate at the expense of the decreasing jet average magnetization, $\sigma \equiv \dot{E}_{EM}/\dot{E}_{KE}$ (purple), before decelerating at the jet bends. The jet average enthalpy, $h \equiv \dot{E}_{TH}/\dot{E}_{KE}$ (orange–red), increases at the jet bends due to energy dissipation. The $\mu \equiv \dot{E}_{TOT}/\dot{E}_{RM}$ parameter (black) decreases due to the jet losing its energy to the ambient medium (via ambient gas displacements and shocks).

large distances, it might lose some details of its internal structure.

4.4. Energy Partition and Dissipation

Figures 3(c)–(d) show radial profiles of quantities, over the *entire* jet cross section, which we define as the relativistic region, $\mu > 3$, to avoid the contamination caused by the mildly magnetized cocoon and weakly magnetized ambient gas. (This is in contrast to Figure 3(b) that considered the averages over the jet core.)

Figure 3(c1) shows various components of the surface-integrated jet energy flux, essentially the power. We normalize

all of the power components by the total power flowing through the entire jet cross section ($\mu > 3$) at $r = 8R_g$, averaged over the duration of the MAD state, $\dot{E}_{MAD} \equiv \langle \dot{E}_{TOT}(r = 8R_g)\rangle_{MAD}$; here, $\langle ...\rangle_{MAD}$ denotes the time average over the MAD state,[11] which we highlighted in purple in Figure 1. The total jet power, $\dot{E}_{TOT}$ (the black line in Figure 3(c1)), remains approximately constant at $r \lesssim 2000R_g$ and drops slightly thereafter, just as the jet starts to bend, as seen in Figure 3(a1). The jet EM power, $\dot{E}_{EM}$ (purple), dominates the jet power at $r \lesssim 2000R_g$, whereas the thermal component of the power, $\dot{E}_{TH}$ (orange–red), steadily increases until, at $r \sim 2000R_g$, it reaches equipartition with $\dot{E}_{EM}$, a telltale sign of energy dissipation (BT16). The increase in $\dot{E}_{TH}$ just as the jet starts to bend most likely comes from the dissipation of EM and KE into heat due to the kink, mixing instabilities, and/or shocks caused by the bend (see Section 4.2).[12] The KE power component, $\dot{E}_{KE}$ (light blue), steeply rises at $r \lesssim 100R_g$, while the RM power component $\dot{E}_{RM}$ (orange) is subdominant compared to the other components.

At $r \lesssim 2000R_g$, $\dot{E}_{KE}$ remains approximately constant, because the jet becomes cylindrical (due to external collimation by the constant-density ambient medium). However, once the jet becomes unstable to the kink instability and develops strong bends, $\dot{E}_{KE}$ drops. At the later time, $t = 71$ k, Figure 3(c2) shows that $\dot{E}_{TOT}$ steeply drops at $r \simeq 800R_g$, right where the jet makes a sharp 90° turn, as seen in the projection on Figure 3(a2). In fact, all of the power components experience similarly sharp drops, since we are only accounting for the radial component of the fluxes, which vanishes. At the location of such drops, which correspond to strong bends, the jet is disrupted and the energy rate does not recover, meaning it is lost. This is anticipated since: (i) when the jets fall apart, they can mix with the ambient medium, lower the specific energy, and so they will not be picked out by our jet criterion $\mu \geqslant 3$; and (ii) the jet bend is spending energy on displacing the surrounding gas.

In Figure 3(d1) we plot the jet area averaged radial profiles of the μ parameter (black), the magnetization, σ (purple), the proper velocity, γv (light blue), and the gas specific enthalpy, h (orange–red). To compute the jet area averaged values, we expressed them through the ratios of jet power components (i.e., using $\dot{E}_{\#}$ in place of $f_{\#}$ in the definitions (13)–(16)). Figure 3(d1) shows that the jet accelerates to relativistic velocities, $\gamma v \simeq 2$ at $r \lesssim 100R_g$ and $\gamma \simeq 3$ at $r \lesssim 1000R_g$. At $r \lesssim 2000R_g$, the jet is still magnetized, $\sigma \gtrsim 2$, the proper velocity remains (on average) relativistic, $\gamma v \gtrsim 3$, and the enthalpy, h, slowly increases, similar to $\dot{E}_{TH}$. Once the jet becomes unstable and develops the bends, the magnetic energy dissipates into heat, until $\sigma \lesssim h$, i.e., until the magnetic energy comes into equipartition with the thermal energy. The KE is also reduced, with the jet decelerating down to the transrelativistic value $\gamma v \simeq 1.7$, as the jet needs to slow down in order to be able to navigate the jet bends (see Section 4.2). In Figure 3(d2), we see a similar behavior as in Figure 3(d1), but with the kink instability happening much closer to the BH, already at $r = 800R_g$. Both the magnetization and proper velocity drop, $\sigma \lesssim h$ and $\gamma v \simeq 1.7$, and the enthalpy h increases.

5. A Turbulent Epilogue

Figure 4(a) shows 3D volume-rendered images of the low-density (purple) jets and the high-density accretion flow (orange). Figure 4(a1) shows the system at $t = 50$ k when it is in the MAD state: the jets are powerful and mostly bend-free, and the accretion flow near the BH shows a disklike structure. Figure 4(a2) shows the system after it has exited the MAD state, where the jet power has decreased by a factor ∼4. The weakened jets appear to have bends originating from wobbles near their launching region. Figure 4(a3) shows jets with extreme bends, misaligned from the BH spin (z-)axis. The accretion flow is also significantly misaligned, compared to Figures 4(a1) and (a2). This shows that the evolution, stability, and destruction of the jets are correlated with the underlying state of the accretion flow near the launching region.

To understand the evolution of the system, we calculate the density-weighted specific angular momentum, $\vec{l} = \vec{r} \times \vec{v} = (l_x, l_y, l_z)$, at a given r. In particular, we compute the magnitude of $\vec{l}$:

$$l(r) = \frac{\iint \rho dA (l_x^2 + l_y^2 + l_z^2)^{1/2}}{\iint \rho dA}. \quad (24)$$

The angular momentum computed this way is appropriate in flat spacetime, $r \gtrsim 10R_g$. We normalize the resulting specific angular momentum with the specific Keplerian angular momentum l_K around a Kerr BH with spin $\vec{a}$ (Shapiro & Teukolsky 1986):

$$l_K(r) = \frac{\sqrt{r}(r^2 - 2a\sqrt{r} + a^2)}{r\sqrt{r^2 - 3r + 2a\sqrt{r}}}. \quad (25)$$

Figure 4(b) shows the magnitude of l/l_K on a spacetime diagram. The three vertical black lines indicate the times of the 3D panels in Figure 4(a). We choose $l/l_K \simeq 0.3$ as a fiducial value to separate the accretion disk from the rest of the gas, which we overplot as a green contour in Figure 4(b). Although initially the gas had zero angular momentum, within several R_g from the BH the frame dragging (Lense & Thirring 1918) due to the BH high spin ($a = 0.94$), combined with large-scale magnetic fields, force the accretion flow to partially corotate with the BH: as a result, the flow develops an azimuthal angular momentum component (see also R21). Additionally, the MRI excites disk turbulence and transports the angular momentum outward, so the disk can grow in size. Indeed, by $t \simeq 50$ k, the accretion disk size has grown up to $50R_g$.

Figure 4(a1) shows that once formed, the jet travels along the BH spin axis (perpendicular to the $x - y$ disk plane, i.e., along the z-direction). Figure 4(c) shows the tilt and precession angles of both the disk and one jet, at $r = 50R_g$ (the dashed black line in Figure 4(b)). We calculate the disk tilt $\mathcal{T}_d$ (orange line) and precession $\mathcal{P}_d$ (orange circles) angles using $\mathcal{T}_d = \cos^{-1}(l_z/l)$ and $\mathcal{P}_d = \cos^{-1}[l_y/(l_x^2 + l_y^2)^{1/2}]$, respectively. To compute the jet tilt and precession angles, we first find the Cartesian coordinates of the jet core centroid, at every radius r, using the magnetization-weighted average of x_j, y_j, and z_j in regions where $\mu > 3$ and $b_p \geqslant b_{tor}$. The jet tilt is then given by $\mathcal{T}_j = \cos^{-1}(z_j/r_j)$ (purple) and the precession angle by $\mathcal{P}_j = \cos^{-1}[y_j/(x_j^2 + y_j^2)^{1/2}]$

[11] Because most of the EM energy flux out of the BH flows through the highly magnetized jets, we have $\dot{E}_{MAD} \approx 0.5\langle L_j\rangle_{MAD}$, where the factor of 0.5 is needed because L_j is the EM power of both jets.

[12] At much smaller distances, close to the jet base, $r \lesssim 100R_g$, highly magnetized inner jet regions can heat up due to the numerical truncation error that affects the smallest energy scale—in this case, the internal energy. However, these effects tend to operate when the internal energy is very small, $\dot{E}_{TH} \lesssim$ few $\times\, 0.01\dot{E}_{TOT}$.

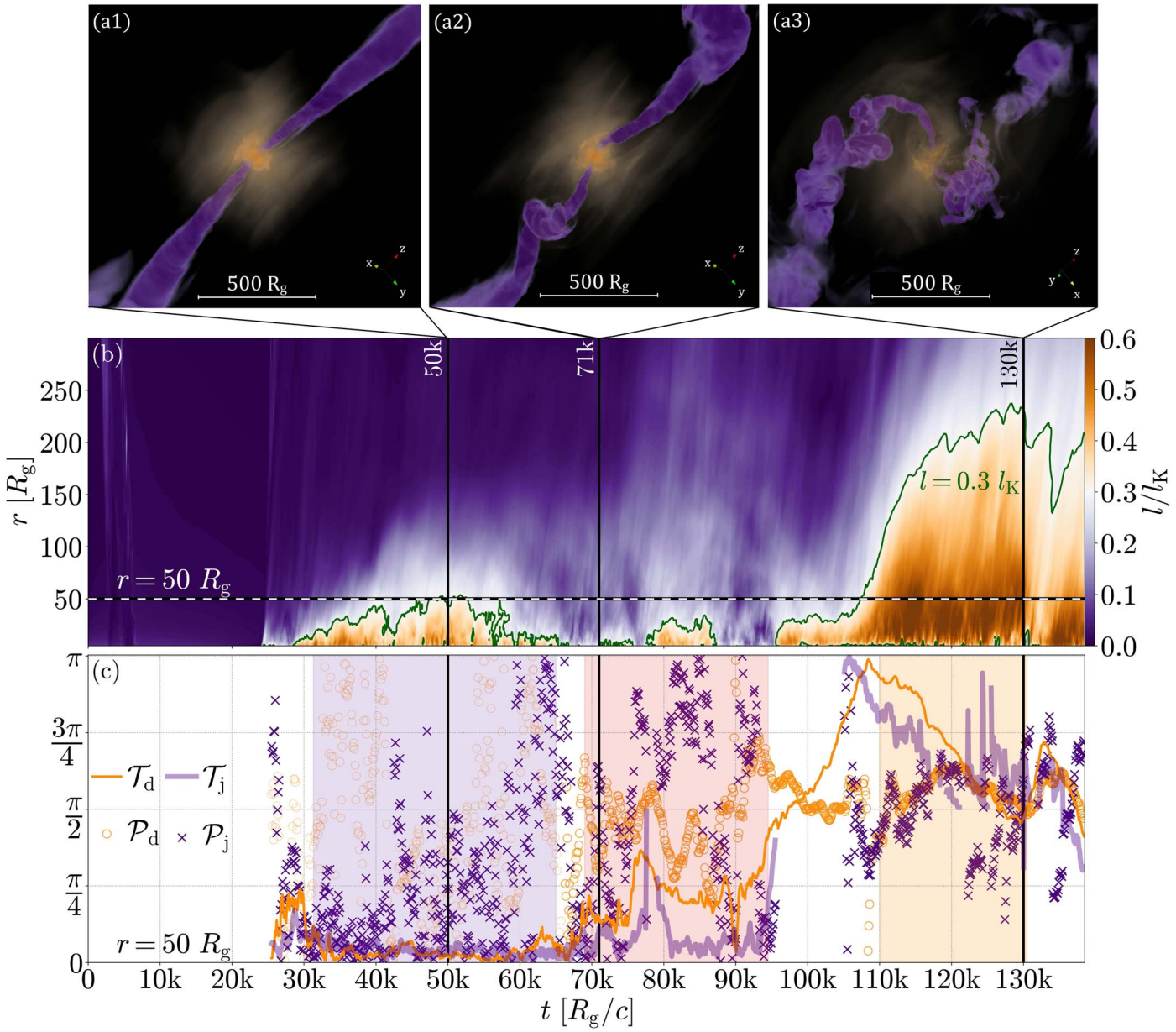

Figure 4. The morphology, strength, and directions of the angular momentum of the accretion flow during the MAD, BAD, and RAD states. (a) We show three distinct 3D volume-rendered images of density. Panel (a1) captures the system during the MAD state, at $t = 50$K, where the jets (purple) follow the direction of the BH's spin, and the accretion disk (orange) lies perpendicular to the jets. Panel (a2) captures the system in the BAD state, at $t = 71$ k, with weakened jets showing strong bends near the BH and getting significantly kinked. Panel (a3) captures the system in the RAD state, at $t = 135$ k. The jets are on average 1 order of magnitude weaker and misaligned from the spin direction. The disk is also significantly tilted, at about $\pi/2$, and precessing, causing significant bends and wobbles in the jets. (b) We plot the density-weighted specific angular momentum normalized to the local Keplerian value in a spacetime diagram. Angular momentum builds around the BH promptly after freefall ($t_{\rm ff} \simeq 22$k) with an average disk of size $10 - 50R_{\rm g}$, chosen for $l \gtrsim 0.3 l_{\rm K}$. Between, 65 k $\leqslant t \leqslant$ 100k, the accreted angular momentum forms intermittent and tilted disks with $l \leqslant 0.3 l_{\rm K}$, which results in intermittent and wobbly jets. After $t \simeq 100$k, the angular momentum starts building up, this time reaching larger radii $\simeq 200R_{\rm g}$; however, near the BH, the intermittent jets push most of the gas away while oscillating wildly, stopping the angular momentum from coherently adding up and stabilizing the jets. (c) We show the tilt and precession angles of the disk and north jet, measured at a distance of $r = 50R_{\rm g}$. During the MAD state (purple shaded), both the tilt of the disk $\mathcal{P}_{\rm d} \lesssim \pi/16$ (orange) and jet $\mathcal{P}_{\rm j} \lesssim \pi/16$ (purple), as they are aligned with the BH spin. The disk precession angle (orange circles), $\mathcal{T}_{\rm d}$, is ill-defined as the disk tilts about the z-axis, while the jet precession angle (purple crosses), $\mathcal{P}_{\rm j} \lesssim \pi/2$, which means it propagates at a preferential direction. Once we transition from the MAD to the BAD state (red shaded), at $t \geqslant 65$ k, the disk's angular momentum has decreased, while its tilt increases, reaching up to $\pi/2$, and rapidly precesses. The jet tries to follow and forms large bends (see Figure 4(a2)) that lead to its destruction. Between 95 k $\lesssim t \lesssim$ 110 k, the disk's tilt goes from $\pi/2$ to π, flipping to retrograde, while the jet is disrupted. During the RAD state, at $t \geqslant 110$ k, the disk flips again, which coincides with the flipping of the magnetic flux on the northern hemisphere, in Figure 1(b). After $t \gtrsim 105$ k, we show the tilt and precession of the counterjet, as it attempts to follow the rocking motion of the disk.

(purple crosses), where $r_{\rm j}^2 = x_{\rm j}^2 + y_{\rm j}^2 + z_{\rm j}^2$. Figure 4(c) shows that during the MAD state (purple shaded) the tilt angle is small, $\mathcal{P}_{\rm d} \leqslant \pi/16$, at $t \lesssim 65$ k: in other words, the angular momentum vector is nearly parallel to the BH spin. For this reason, the disk precession angle, $\mathcal{P}_{\rm d}$, is ill-defined and we lower its opacity to minimize clutter. The jet tilt is, on average, similar to the disk tilt, with $\mathcal{T}_{\rm j} \leqslant \pi/16$. The jet precession angle shows high-amplitude variability, but on average clusters around $\mathcal{P}_{\rm j} \lesssim \pi/2$. This means

that the jet on average has a preferred direction that is distinctly different than the rotational axis of the BH: indeed, Figure 4 shows that both jets are skewed sideways, toward the y-axis.

At $50\,\mathrm{k} \lesssim t \lesssim 65\,\mathrm{k}$, the radial extent of the disk shrinks down to $\sim 10R_\mathrm{g}$, and by the end, it disappears, as the MAD state ends. This hardly seems like a coincidence, and we suggest that the system exits the MAD state when the accretion flow loses the rotational support. But what can cause the loss of angular momentum in the disk? It is possible that once launched, the jets perturb the infalling gas and induce turbulence and vorticity, with the angular momentum, on average, misaligned with the BH spin vector. Once the misaligned angular momentum reaches the disk, it can cancel out the disk's coherent angular momentum, which was relatively low, to begin with, due to the limited disk radial extent ($R_\mathrm{disk} \simeq 50R_\mathrm{g} \ll R_\mathrm{B} = 1000R_\mathrm{g}$). Moreover, strongly magnetized disks can launch winds that carry the angular momentum outward (Blandford & Payne 1982) and can further reduce the disk's angular momentum. Whatever the case, the disk of small size, $\lesssim 10R_\mathrm{g}$, cannot support a jet with large-scale winds. The jet is left exposed to violent interactions with the ambient medium, for which the winds would normally act as a cushion. Additionally, the magnetic flux on the BH, once held by the disk, leaks out (Figure 1(b)) and the power of the jet decreases (Figure 1(c)), making the jets more easily bendable.

From here on, the system's behavior changes drastically: at $t \gtrsim 65$ k, our quasi-steady MAD state transitions to a state dominated by the accretion of gas with a continuously varying direction of the angular momentum vector. At $69\,\mathrm{k} \lesssim t \lesssim 95$ k, the disk tilt increases and the disk starts precessing, while the angular momentum magnitude decreases. The flow with such low angular momentum is Barely A Disk, which we will refer to as the BAD state. The weakened and slower jet is now more affected by the presence of the ambient gas and, more specifically, the precessing and tilting disk starts twisting the jet into a helix: this is similar to when one shakes the end of a rope in a circular fashion, creating circular waves that are transmitted along the rope. Around $t = 78$ k, the jets transiently fall apart (due to the shutoff of jet power at the BH; Figure 1(c)). Figure 4(b) shows that subsequently, a short-lived disk of size $\sim 30R_\mathrm{g}$ forms at $78\,\mathrm{k} \lesssim t \lesssim 85$ k. Figure 1(c) shows that the jets remain active until $t \simeq 95$ k.

At $95\,\mathrm{k} \leqslant t \leqslant 110$ k, the disk gradually flips upside down and changes its sense of rotation from prograde ($\mathcal{T}_\mathrm{d} \sim 0$, rotating in the same sense as the BH) to retrograde ($\mathcal{T}_\mathrm{d} \sim \pi$, rotating in the opposite sense to the BH).[13] This causes the jets to weaken, bend dramatically, and disrupt. We will refer to this state as the Rocking Accretion Disk (RAD), where the accretion of gas with highly tilted angular momentum is capable of flipping the disk upside down. We highlight a specific part of the RAD state, during $110\,\mathrm{k} \leqslant t \leqslant 130$ k, where the disk gradually flips back to the prograde configuration, but stops at $\mathcal{T}_\mathrm{d} \simeq \pi/2$. Interestingly, when measured at $r = 15R_\mathrm{g}$ (not shown here), the tilt decreases all the way down to $\mathcal{T}_\mathrm{d} \simeq \pi/4$. The absolute dimensionless magnetic flux, ϕ_BH, remains approximately constant during this transformation. In contrast, the magnetic flux through the northern hemisphere, ϕ_N, smoothly changes sign in phase with the disk tilt angle changes: this is precisely the behavior we would expect if the entire disk–jet system underwent a flip. During this stage of the simulation, we witness a large angular momentum inflow (Figure 4(b)), leading to an increase in the disk size to $\sim 200R_\mathrm{g}$. The formation of an accretion disk, which grows in size, deprives the BH of the gas and suppresses the BH accretion rate. Although 15 times less powerful than in the MAD state, the weaker, intermittent, and continuously reorienting jets fail to pierce through the infalling gas and are forced to bend around it: as seen in Figure 4(a3), they efficiently couple their energy to the infalling gas and additionally reduce BH accretion. This results in BH mass accretion rate suppression to $\dot{M}/\dot{M}_\mathrm{B} \sim 1.7\%$, similar to the MAD state.

[13] After the disk changes its orientation, we show the tilt and precession of the counterjet.

6. External versus Internal Kink

Figure 5 shows a time series of jet snapshots, illustrating the propagation of the jets and the growth of the kink instability during the early time in our simulation, in the MAD state ($31\,\mathrm{k} \leqslant t \leqslant 65$ k): the color shows the proper velocity, γv, projected along the y- and x-directions[14] in the left and right columns, respectively. We identify two early-time features, $E1$ and $E2$, which propagate along the jet, and we study how they grow due to the kink instability. We pick these regions by (i) visually searching for significant jet bends, or wiggles, and/or (ii) identifying jet regions with low values of the stability parameter, $\Lambda \lesssim 2$ (e.g., in an animation of Figure 3(b)). In both projections, the jet exhibits multiple wiggles along its length, which originate near the jet launching region and propagate out. Such wiggles can emerge due to the stochastic nature of BH accretion and wind–jet interactions (see, e.g., Figure 4(c)). Both the $E1$ and $E2$ features start out as small-scale wiggles and propagate out to $r \simeq 1500R_\mathrm{g}$. The jet remains mostly straight and maintains a relativistic velocity, $\langle \gamma v \rangle \simeq 3$. Such powerful jets as this one, in the MAD state, can accelerate to and sustain relativistic velocities ($\gamma v \gtrsim$ few): the relativistic motion stabilizes the jets against kink instability due to relativistic time dilation (see Equation (18), which has the Lorentz factor in the numerator). However, as the jets propagate out to larger distances in the flat density distribution, they become increasingly unstable (Section 4.1). Indeed, after reaching $r \simeq 1500R_\mathrm{g}$, the jets develop unstable regions, $\Lambda \lesssim 2$ (Figure 3): this implies that the kink instability growth timescale becomes comparable to the dynamical time of the jet, and the jet bends grow in amplitude. Indeed, both the $E1$ and $E2$ features develop stronger jet bends that force the jet to slow down to $\langle \gamma v \rangle \simeq 1.7$ (see Equation (22)). These bends continue to grow both in amplitude and spatial scale and end up essentially breaking up the jet into two segments, as seen in Figure 5(d) for feature $E1$ and in Figure 5(f) for feature $E2$. To calculate the propagation speed of the $E1$ and $E2$ features, we fit straight lines through them, as we show in Figure 5. Both features propagate along the jet at $v/c \simeq 0.82 - 0.85$, which is comparable to, but slightly lower than, the jet velocity.

We have just discussed how in the MAD state the jets developed unstable features: jet bends that propagate outward, while slowly growing in amplitude. However, the jets managed to maintain their outward motion most of the way to the jet head. We also saw in Figures 2 and 3 that the jets globally disintegrated shortly after the system exited the MAD state at $t \simeq 65$ k. Can we devise a criterion to *predict* when such

[14] We accomplish such projections by working in the original 90° tilted frame where the jets propagate in the x-direction. The projections are then in the θ- and φ-directions, respectively.

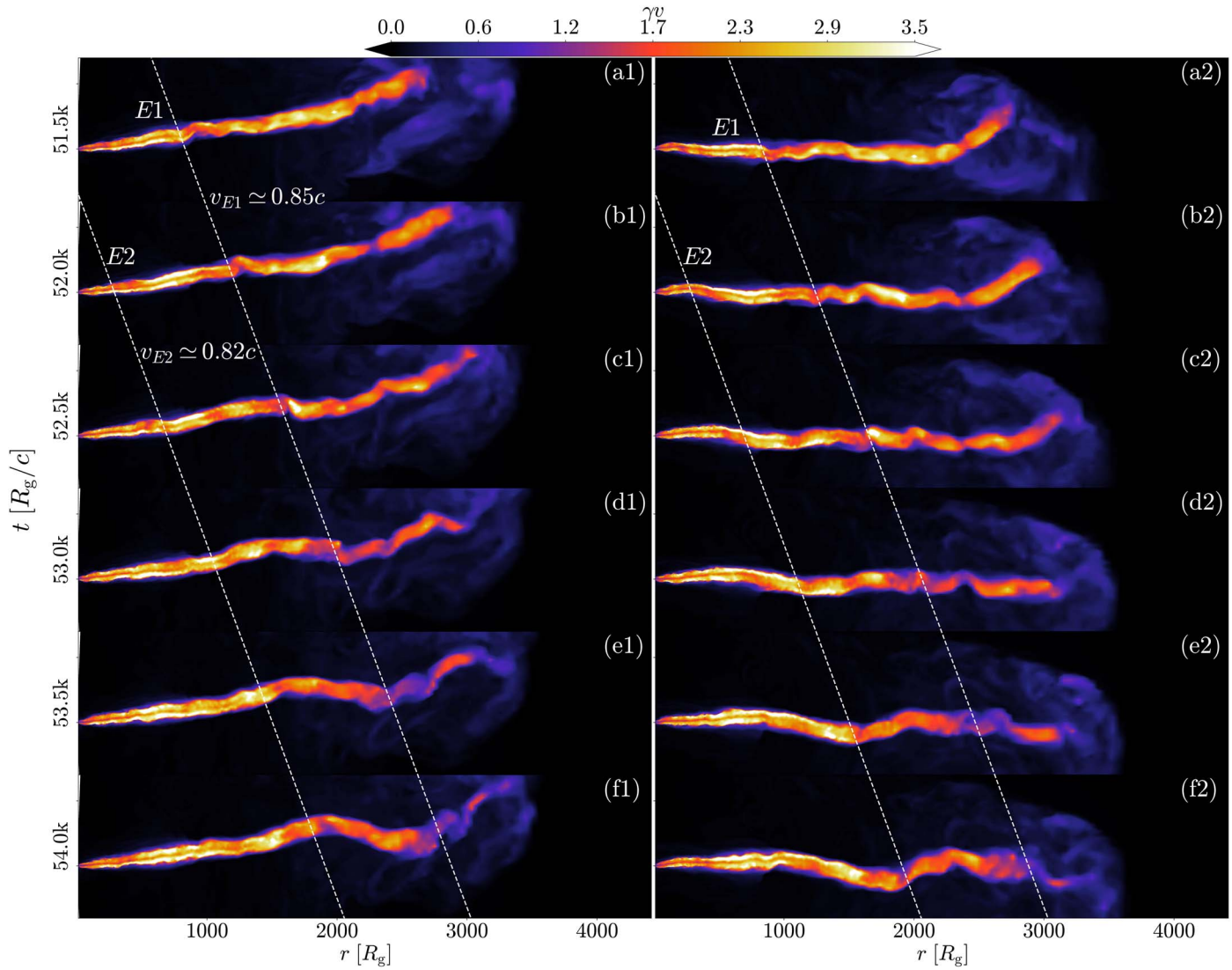

Figure 5. Early-time MAD jet exhibits multiple small-amplitude bends and a major bend located at $r \simeq 1500R_g$. An animation of this figure is available and on YouTube. The animation runs from $t = 5.00 \times 10^4 R_g/c$ to $t = 8.00 \times 10^4 R_g/c$. The real-time duration of the animation is 29 s. The left and right columns show the jet's proper velocity, γv, projected along the y- and x-directions, respectively. We fit a straight line through features along the jet, which show wiggles ($E1$, $E2$), and which we follow at different times to observe their growth. The slope of the white dashed line gives the propagation speed of the wiggles. For both the $E1$ and $E2$ features, the velocity is approximately $v/c \simeq 0.82$–0.85. The wiggles, which can act as a seed for the kink instability, originate from the jet tilting and precessing about the BH spin. However, the fluid velocity is relativistic, $\gamma v \simeq 3$, and the jet fluid does not have enough time to become kink-unstable, not until it reaches the distance of $r = 1500R_g$, where it becomes globally unstable.

(An animation of this figure is available.)

catastrophic jet destruction is bound to happen? BT16 derived a simple analytic approximation for a global jet stability parameter that evaluates the ability of the kink mode to grow on the jet periphery, leading to a global deformation of the jet body. For a jet of power, L_j, which moves through an ambient medium of constant density, ρ_a, at a Lorentz factor, $\gamma = 1/\sqrt{1 - v^2/c^2}$, the stability parameter at the jet head distance, $r = r_h$, is:

$$\Lambda_h \propto \left(\frac{L_j}{\rho_a r_h^2 \gamma^2 c^3}\right)^{1/6} \times \frac{\sqrt{v}}{v_A}\,, \tag{26}$$

where for simplicity we have omitted constant prefactors.

Can Equation (26) predict the global jet disintegration we observe in our simulations? Upon exiting the MAD state and turning BAD, at $t = 69$ k, the jet power drops fourfold (Figure 1(c)). At the same time, the jet Lorentz factor decreases from $\langle \gamma v \rangle \simeq 3$ to $\langle \gamma v \rangle \simeq 1.7$, but v_A remains roughly unchanged (compare Figures 3(b1) and (b2)). The distance to the jet head, r_h, does not change significantly, because the drop in power occurs over a short timescale ($\Delta t \sim 5$ k) and leaves the jet head little time to advance (compare Figures 2(b) and (c)). As a result, the stability parameter drops by an order unity factor, $\Lambda_{MAD}/\Lambda_{BAD} \simeq 1.1$.

Why does the stability criterion, Equation (26), not capture the global jet instability we observe in the simulation? Figure 6 shows a time series of jet images at a later time, $68\,\mathrm{k} \leqslant t \leqslant 70.5$ k, after the end of the MAD state and right up until the time when the jet becomes strongly kinked and globally unstable, a precursor to its global destruction. Figures 6(a)–(c) show a relativistic jet (yellow), $\langle \gamma v \rangle \simeq 3$, which eventually slows down to transrelativistic speed (orange), $\langle \gamma v \rangle \simeq 1.7$, in

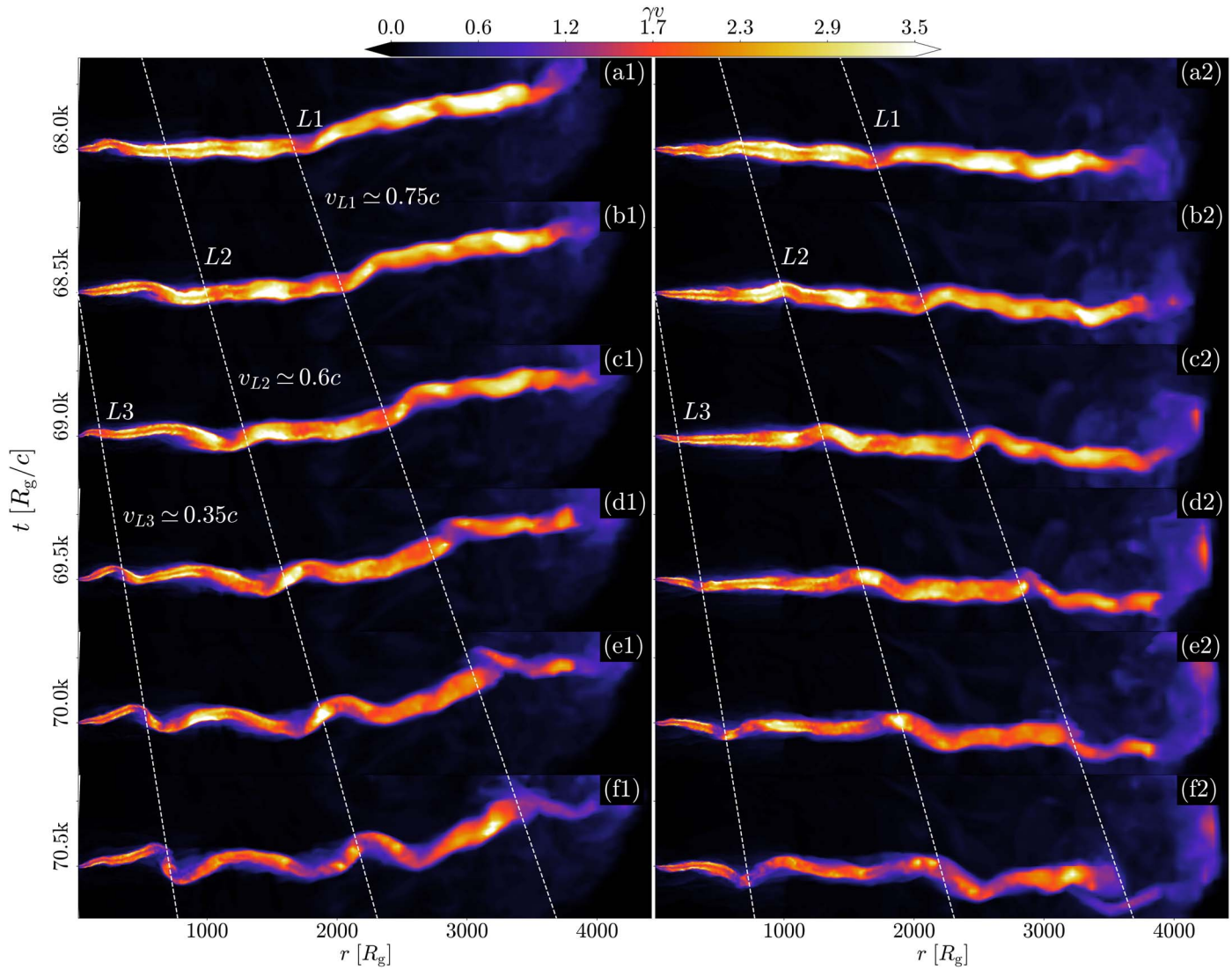

Figure 6. The BAD jet gets progressively disrupted, with small bends fully developing into large bends. Similar to Figure 5, the color shows the proper velocity, γv, and the two columns are the projections along the y- and x-directions, respectively. This jet has an average power four times smaller than the average power during the MAD state. The drop in power is also associated with the tilt of the disk slowly increasing, as shown in Figure 4(c). The power drop leads to jets that cannot efficiently accelerate to previously relativistic velocities, and as the jets follow the tilt of the disk, they run into the ambient medium, shock, and decelerate even more (see Figure 3(b2)). An external kink starts affecting the jet bends. As the bends get progressively larger, the fluid can become internally kink-unstable, leading to the "breaking" of the jet. We fit a straight line through regions that develop large bends, $L1$, $L2$, and $L3$, and we estimate the wiggle propagation velocity from the slope. The $L1$ spot follows a bend developed during the end of the MAD state, when the fluid was mostly stable to the kink. At $r \simeq 2000R_g$, a bend develops and the wiggle grows without significantly bending the jet, until the jet fluid smashes at the head. The estimated propagation speed is slightly smaller than the MAD equivalent, at $v \simeq 0.75c$. The $L2$ spot propagates slower than $L1$, at $v \simeq 0.6c$, and the wiggle amplitude is noticeably larger. Finally, $L3$ is launched well into the weaker jet phase, and the jet bend becomes nonlinear until the full jet disruption at $r \simeq 800R_g$. The $L3$ wiggle propagates at $v \simeq 0.3c$, significantly slower than either $L1$ or $L2$, due to the fact that the large-amplitude bends launched near the BH interact with more ambient gas, which slows it down even more.

Figures 6(d)–(f). The dark purple regions are locations where $\langle \gamma v \rangle \lesssim 1$ and where the jet is getting disrupted. We identify three bend features ($L1$, $L2$, and $L3$) that grow in time. The feature $L1$ is one of the last features to be ejected during the MAD state. In Figures 6(a1) and (a2), the jet is mostly straight, apart from the large bend at $r \simeq 2000R_g$: this is the bend associated with the $L1$ feature, and it grows as the feature approaches the jet head. The propagation speed of $L1$ is $v_{L1} \simeq 0.75c$, comparable to what we found for unstable regions at earlier times, as seen in Figure 5. The $L2$ feature was ejected after the system exited the MAD state and after the jets weakened and became unstable: this enables the $L2$ bend to grow, as seen in Figure 6(b2). Figures 6(a)–(d) show that the $L2$ feature propagates out and grows in amplitude with a propagation speed of $v_{L2} \simeq 0.6c$, which is lower than that of the $L1$ feature. Ejected at an even later time, the $L3$ feature starts out as a bend of high amplitude already at $r \lesssim 500R_g$, in Figure 6(c). Its propagation speed, $v_{L3} \simeq 0.35c$, is the lowest among all E and L features and is, therefore, the most unstable. Indeed, Figure 6 shows that the $L3$ feature grows to become a 90° jet bend, at $r \simeq 800R_g$, which eventually globally disrupts the jet.

Summing up, we are witnessing a runaway growth of the kink instability that generates large-scale, strong jet bends. This implies that Equation (26), for some reason, does not apply to our weakened jets in the BAD state (the red shaded region, $69\,\mathrm{k} \leqslant t \leqslant 95$ k, in Figure 1). Namely, once the system enters this state, the linear stability analysis (Equation (26))

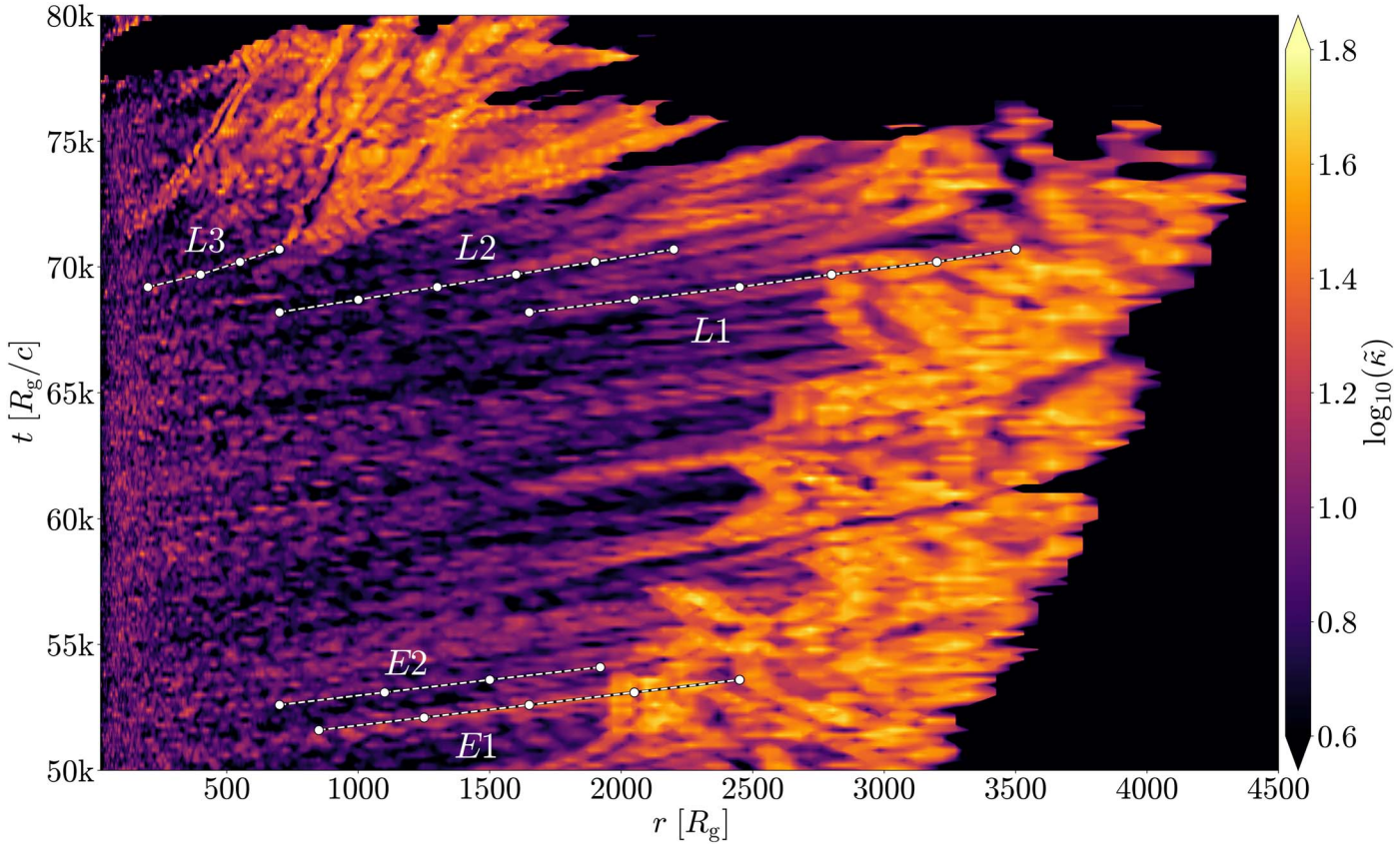

Figure 7. The spacetime diagram shows that the normalized jet curvature, $\tilde{\kappa}$, grows due to the kink instability as it advects along the jet. We overplot the tracks of the jet features in the MAD state ($E1$, $E2$) and BAD state ($L1$, $L2$, $L3$), also seen in Figures 5 and 6. The slopes of these tracks give us the propagation speeds of the features. During the MAD state, the large-scale bends tend to develop at $r \simeq 1500R_g$ and propagate to larger scales at roughly the speed of the jet fluid, $v \sim 0.8c$, as the jet powers the cocoon. The cocoon outer boundary (the rightmost extent of the boundary of the orange region) expands at $v \simeq 0.05c$, i.e., much slower than the jet features. After the flow exits the MAD state ($t = 65$ k) and enters the BAD state ($t = 69$ k), the jet power drops and strong jet bends form at much smaller distances, $r/R_g \simeq 500$–1000, and propagate at much slower speeds, $v \sim 0.3c$ (e.g., for feature $L3$). Eventually, the jet is globally destroyed, at $t \simeq 78$ k, as its power vanishes (Figure 1(c)).

underpredicts the growth of the global kink. What is missing from the linear stability criterion, Equation (26), are the nonlinear effects that combine to cause a catastrophic runaway of the instability. Namely, the fluctuations in the disk tilt (Figure 4(c)) cause the jets to wobble around the BH axis and propagate in directions offset from the jet predrilled path. This causes the jets to plow up the gas along new paths, through the shocked cocoon material. Because the cocoon was generated at earlier times, when the jets were four times more powerful, the weakened jets have difficulty displacing the material and get deflected: this causes the jets to bend and slow down (Equation (22) and Figures 3(a1) and (b1)). The slower velocity accelerates the kink (and bend) growth and further slows down the jet propagation. As a result, such interactions lead to a runaway slowdown not only of the jet fluid, but also of the jet bends (Figure 6). In fact, the global kink instability we are witnessing here grows in the frame of the bends, which move slower than the jet fluid and hence become more susceptible to the kink instability. This is an example of a nonlinear evolution of an *external* kink instability, which deforms the jet interface with the ambient medium. This is different than the *internal* kink instability, which works on disrupting the jet core, but leaves the jet–ambient medium interface intact. The two flavors of the kink instability can coexist: for instance, the growth of the external kink instability can trigger the internal kink instability.

To study the nonlinear evolution of the global, external kink instability in a more systematic way, we present in Figure 7 a spacetime diagram, where the color shows the logarithm of the dimensionless jet curvature,

$$\tilde{\kappa} = r\kappa = r\left|\frac{d\vec{s}}{dr}\right|, \tag{27}$$

where κ is the dimensional jet curvature and $\vec{s}$ is a unit vector parallel to the jet. High values of the dimensionless curvature (yellow) indicate strong bends, whereas low values (black) correspond to mostly straight jets. We see that even at small distances, $r \lesssim 1000R_g$, the jet develops multiple bends along its length, due to the interactions with the ambient medium and disk winds. In Figure 7, we plot the tracks of all features we identified in Figures 5–6: the slopes of the tracks give the propagation speeds of the features. During the MAD state, $t \lesssim 65$ k, the jet on average is mostly straight, and the bends travel at nearly the same speed as the jet fluid. If we follow the $E1$ and $E2$ features, they develop significant (orange) bends, at $r \simeq 1500R_g$, where the dimensionless curvature reaches $\log_{10}(\tilde{\kappa}) \gtrsim 1.5$.

Farther away, at $r \gtrsim 2000R_g$, the jets get even more twisted: they become globally unstable, break apart, and energize the cocoon. Inflated by the jets, the cocoon expands at a nonrelativistic speed of $v \simeq 0.05c$, as revealed by the slope of

the jet–cocoon boundary, which is seen as the orange–black transition on the right of Figure 7. In fact, Figure 7 reveals that the entire bright orange region of the strongest jet bends shifts in time toward larger radii. This suggests that the proximity to the cocoon exacerbates jet bends: cocoon convective motions can displace and bend the jets sideways. Indeed, one can visually identify such convective cocoon motions in the animation of Figure 2 (see the figure caption for a link). Consistent with this picture, once the cocoon expands out to larger radii, the jets manage to avoid significant bends out to larger radii as well: the radius beyond which the jets start to show significant bends slowly increases from $r \simeq 1500R_{\rm g}$ at $t = 50$ k to $r \simeq 3000R_{\rm g}$ at $t \simeq 68$ k, just before the MAD state ends and the jets become globally unstable.

Visually following the slope of the "late-time" track of feature $L1$ in Figure 7, we estimate the propagation speed of jet bends prior to disruption, $v_{L1} \simeq 0.75$ c, which is consistent with the best-fit values in Figure 5. However, once the MAD state comes to an end, at $t \simeq 65$ k, the jet power drops. This causes each subsequent feature to travel at a slower speed, as indicated by the steepening of the slopes, decreasing to $v_{L2} \simeq 0.6c$ and eventually to $v_{L3} \simeq 0.35c$. This is consistent with the feature propagation speeds we measured in Figure 6. At $t \gtrsim 70$ k, the jet develops extreme bends and shortens to $r \lesssim 2000R_{\rm g}$, before globally disrupting at $t \simeq 78$ k.

7. Discussion and Conclusions

We study large-scale jet propagation and survival in global 3D GRMHD simulations of weakly magnetized, zero-angular-momentum gas accretion onto rapidly spinning BHs, $a = 0.94$. The gas accretes from the Bondi to the event horizon radius, traversing the largest scale separation to date, $R_{\rm B} = 10^3 R_{\rm g}$, in a single 3D GRMHD simulation. Over time, the gas drags in from the ambient medium large-scale vertical magnetic flux, which readily accumulates on the BH and launches powerful relativistic collimated jets.

Although initially our accretion flow started out without any angular momentum, as the accretion flow goes MAD, it forms an accretion disk of size $\sim 50R_{\rm g}$ (see also R21; K23). Thus, no pre-existing accretion disk is required to form jets and collimate them via winds, as long as the BH is rapidly spinning and has accumulated dynamically important large-scale poloidal magnetic flux on its event horizon. Interestingly, the MAD state achieved in our simulation is long-lived: its duration of $\Delta t = 34$ k is three times as long as the total simulation duration in R21 and about half as long as the simulation duration in K23, where in both cases the system only transiently enters the MAD state. Although our MAD state lasts comparatively longer, it still has a finite duration: the BH eventually loses the large-scale magnetic flux and the jets fall apart. The MAD state ends in a fashion similar to that observed by R21 and K23. Afterward, once our jets transiently reappear, they do not reach beyond the Bondi radius.

To explore the origin of the differences between different groups, we repeated our simulation at a reduced scale separation, $R_{\rm B}/R_{\rm g} = 10^2$, to match that of R21 (see Appendix C). We carried out the simulation for $t \simeq 110$ k, a factor of ~ 5 longer than R21. The system turns MAD ($\phi_{\rm BH} \gtrsim 50$) at $70\,{\rm k} \lesssim t \lesssim 100$ k, which suggests that the MAD state can establish itself, but it might take longer simulation durations in order to witness it. Why do MADs in the simulations of K23 survive for a rather short duration? One possibility is that our simulations contain more magnetic flux closer to the BH: although both simulations start with $\beta = 100$ gas, we use a constant vertical field, $B_z = $ constant, which results in the enclosed poloidal magnetic flux scaling as $\Phi \propto B_z r^2 \propto r^2$. In contrast, K23 use a parabolic-like field, $B_z \propto r^{-1}$, whose flux has a flatter radial profile, $\Phi \propto B_z r^2 \propto r^1$. Thus, out to the same distance, our simulations contain a larger flux reservoir. It is possible that this allows our simulations to transport the magnetic flux to the BH at a higher rate than the BH loses it due to the magnetic flux eruptions. Additionally, they have an adiabatic index $\Gamma = 4/3$, which describes radiation-dominated gas. Because this makes the gas more compressible, this can reduce the disk scale height and make it harder for the disk to hold on to the magnetic flux on the BH.

Apart from the early-time transient phase, our MAD jets carry the maximum power and extract BH rotational energy at high efficiency, $\eta \simeq 190\%$. The jets reach distances of $r \gtrsim 4000R_{\rm g}$, or 3.5 orders of magnitude in scale separation. In the inner $\sim 50\%$ of the jet length, $r \lesssim 1500R_{\rm g}$, the jets remain mostly bend-free, but they exhibit variability in their tilt and precession angles (Figure 4(c)). The MAD eruptions, along with disk turbulence, give rise to jet wobbles that can propagate outward (see the animation of Figure 5). In Figure 3, during the MAD state, the jets exhibit direction/directional variability on the order of $\Delta t \simeq 10^4 R_{\rm g}/c \simeq 10$ yr, scaled to M87. We offer this as an observational alternative to Lense & Thirring (1918) precession of a misaligned disk–jet system (Cui et al. 2023). Farther out, the jets develop twists and bends, as they become kink-unstable. Magnetic energy dissipates into thermal energy, a process that can power high-energy teraelectronvolt flares (Giannios et al. 2009; Schoeffler et al. 2023). The jet magnetization drops until the magnetic fields reach equipartition with the gas thermal energy. Multiple locations along the jets show signs of recollimation and/or oblique shocks, associated with small-scale bends of the jets. To interpret this association, recall that at the recollimation point, the fluid pinches and decelerates, which leads to a drop in the local stability parameter, Equation (26), and explains how marginally stable jets become kink-unstable and twist as a result.

The fact that the jets can reach $r \simeq 1500R_{\rm g}$ without getting globally disrupted is not trivial. R21 find that their jets become kink-unstable at $r \simeq 200$–$400R_{\rm g}$. Using Equation (26) to extrapolate to larger Bondi radii and assuming a density profile of $\rho \propto r^{-1}$ within the Bondi radius, they predict that for $R_{\rm B} \gtrsim 800R_{\rm g}$, jets should become kink-unstable. Because observations show many jets survive out to much greater distances, this would suggest that such jets cannot be powered by low-angular-momentum accretion. Surprisingly, our jets make it out to $r \simeq 1500R_{\rm g}$ without significant global bends. One possible reason for this difference is that when our jets first form, they navigate a steeper density profile, $\rho \propto r^{-3/2}$, than the one established at late times due to feedback processes, $\rho \propto r^{-1}$. The steeper profile makes it easier for the jets to escape unscathed (BT16). Another difference is that soon after jet launching, the accretion flow goes MAD and maximizes the jet power. It is possible that once our system exits the MAD state and the jets transiently shut off, they would struggle to make it out to the same distances even if they went MAD again, because the feedback causes the ambient density profile to flatten, $\rho \propto r^{-1}$, at late times.

At $50\,{\rm k} \lesssim t \lesssim 65$ k, the MAD disk shrinks in size down to $\sim 10R_{\rm g}$, the MAD state terminates ($\phi_{\rm BH} < 50$), and the mass

accretion rate increases. Initially, the jet power stays roughly constant, before dropping. Without the disk wind to shield the jets, the infalling gas slams into and bends them. The bends propagate out along the jets in a spiral pattern. Once the jet power drops, the mass accretion rate increases even further, and the system enters the BAD state at $69\,\mathrm{k} \lesssim t \lesssim 95\,\mathrm{k}$. During this state, the jet becomes even more susceptible to bends, which are amplified by the external kink instability: in fact, the bends grow nonlinear, experience drag against the cocoon material, and slow down. This leads to a runaway growth of the bends that twists the jets into a helix. Figure 3(a2) shows that eventually the instability grows nonlinearly and breaks up the jet into segments. Because each segment is no longer constrained lengthwise by the formerly adjacent jet segment, it is free to expand longitudinally and inject part of its energy into the cocoon, resulting in a dramatic drop in jet energy flux at the beginning of each segment. We show that the global stability criterion, Equation (26), fails to predict the destructive instability growth in the jets because it does not capture nonlinear effects. In contrast, the local linear stability criterion, Equation (20), when applied to the result of nonlinear jet evolution, still correctly predicts the severity of the instability. Our analysis demonstrates the importance of global long-duration numerical modeling to reveal global jet instabilities and the associated dissipation that would otherwise be missed by global linear stability criteria.

As the system went MAD, the jets reached the maximum energy efficiency and suppressed the accretion rate by a factor of ∼70: only a tiny fraction, $\dot{M}/\dot{M}_{\rm B} \simeq 1.5\%$, of the Bondi accretion rate reached the BH, and the feedback (e.g., by BH-powered jets and disk-powered winds) ejected the remaining 98.5% of the gas. L22 used an identical setup, except for including nonzero angular momentum in the ambient medium (with circularization radius $R_{\rm circ} = 30R_{\rm g}$), and found similar levels of $\dot{M}$ suppression. This suggests that most of the feedback is done by the powerful jets, as opposed to disk winds.

Indeed, during the BAD state ($69\,\mathrm{k} \leqslant t \leqslant 95\,\mathrm{k}$), Figure 1(a) shows that the mass accretion remains roughly constant, $\dot{M}/\dot{M}_{\rm B} \simeq 5\%$, despite the formation of an accretion disk at $78\,\mathrm{k} \lesssim t \lesssim 86\,\mathrm{k}$. The average outflow efficiency is $\eta \simeq 15\%$, with weak jets that mainly go through the predrilled path from the prior large-scale jets. In fact, we see that $\dot{M}$ transiently increases whenever the jet power vanishes, e.g., at $t \simeq 78$k and $95\,\mathrm{k} \lesssim t \lesssim 105\,\mathrm{k}$. This indicates that it is the jets, especially in the MAD state, that dominate the $\dot{M}$ suppression, as opposed to the rotationally supported disk and its wind.

For the rest of the simulation, $t \gtrsim 95$ k, the system enters the RAD state, where the accreted material brings in gas with an angular momentum vector that is misaligned with respect to the BH spin vector. Newly formed intermittent and weaker jets do not leave the Bondi radius intact, but promptly get disrupted, leaving behind weakly magnetized buoyant bubbles. When the jets are not active, the mass accretion rate can reach all the way up to $\dot{M}/\dot{M}_{\rm B} \simeq 10\%$. There are periods where the intermittent and weaker jets, along with the formation of an ephemeral misaligned accretion disk, suppress the mass accretion rate down to values in the MAD state. For example, during $110\,\mathrm{k} \lesssim t \lesssim 130$ k, the mass accretion rate averages at $\dot{M}/\dot{M}_{\rm B} = 1.7\%$, while the jet power is weaker compared to the MAD values by ∼15. The outflow efficiency averages at $\eta = 11\%$, while the normalized magnetic flux at $\phi_{\rm BH} = 18$.

During the MAD state, the powerful relativistic jets ($\gamma \simeq 4$) form extensive lobes and hotspots similar to FRIIs. During the RAD state, the jets disrupt at their base, form intermittently, and propagate more slowly ($\gamma \simeq 2$) and in varying directions, without ever making it out of the Bondi radius ($r \lesssim 800R_{\rm g}$). This is similar to FR0 jets that feature mildly relativistic speeds and small sizes ($r \lesssim 1$ kpc), which make them hard to observe. For the first time, in a GRMHD simulation, we are witnessing an FRII jet transition into an FR0 jet. This suggests that FR0s are abundant in environments with low angular momentum. Even though such systems are capable of creating FRI or FRII jets, if the disk loses its angular momentum and shrinks, the system inevitably turns BAD and/or RAD. The jets, which are globally destroyed during the transition from MAD to BAD, might be the source of the γ-rays observed by a handful of FR0s (Paliya 2021), because our simulated jets dissipate a significant amount of EM energy into heat, which can power copious particle acceleration. Thus, jets in the BAD and RAD states might be significant contributors to the isotropic γ-ray background, the diffuse neutrino background (detectable by IceCube), and the ultra-high-energy cosmic rays. We will explore the radiation signatures of a globally kink-unstable jet, as well as the FR0 jets, in a follow-up paper.

Acknowledgments

A.L. wants to thank Nicholas Kaaz, Danat Issa, and Amy Secunda for their fruitful ideas and discussions for this work. We would like to thank the anonymous referee for the helpful comments and suggestions that have helped to improve the manuscript. O.G. is supported by the Flatiron Research and CIERA Fellowships. O.B. was supported by ISF grants 1657/18 and 2067/22, a BSF grant 2018312, and an NSF-BSF grant 2020747 (O.B. and A.T.). J.J. and A.T. acknowledge support from the NSF AST-2009884 and NASA 80NSSC21K1746 grants. H.Z. was supported by NASA under award number 80GSFC21M0002. A.T. was supported by NSF grants AST-2107839, AST-1815304, AST-1911080, AST-2206471, and OAC-2031997. Support for this work was provided by the National Aeronautics and Space Administration through Chandra Award Number TM1-22005X issued by the Chandra X-ray Center, which is operated by the Smithsonian Astrophysical Observatory for and on behalf of the National Aeronautics Space Administration under contract NAS8-03060. The authors acknowledge the Texas Advanced Computing Center (TACC) at The University of Texas at Austin for providing HPC and visualization resources that have contributed to the research results reported within this paper via the LRAC allocation AST20011 (http://www.tacc.utexas.edu). This research used resources from the Oak Ridge Leadership Computing Facility, which is a DOE Office of Science User Facility supported under Contract DE-AC05-00OR22725. An award of computer time was provided by the ASCR Leadership Computing Challenge (ALCC), Innovative and Novel Computational Impact on Theory and Experiment (INCITE), and the OLCF Director's Discretionary Allocation programs under award PHY129. This research used resources of the National Energy Research Scientific Computing Center, a DOE Office of Science User Facility supported by the Office of Science of the U.S. Department of Energy under Contract No. DE-AC02-05CH11231 using NERSC award ALCC-ERCAP0022634. This research used resources of the National

Energy Research Scientific Computing Center (NERSC), a U.S. Department of Energy Office of Science User Facility located at Lawrence Berkeley National Laboratory, operated under Contract No. DE-AC02-05CH11231 using NERSC ERCAP award m2401 for 2022 and 2023.

Appendix A
Fluid-frame Magnetic Fields

Due to relativistic effects, such as aberration, we need to appropriately boost the lab-frame magnetic fields to compute the fluid-frame magnetic fields. We use the definitions

$$b^t = B^i u_i, \tag{A1}$$

$$b^i = \frac{B^i + u^i b^t}{u^t}. \tag{A2}$$

The four-vector b^μ is the fluid-frame magnetic field that is comoving with the four-velocity u^μ. Since the linear analysis of the growth of the kink instability distinguishes the poloidal and toroidal components of the fields, we aim to do the same. In an idealistic setup, the jet would mostly propagate along the z-axis, and one would write the magnetic field as $\boldsymbol{B} = \boldsymbol{B}_p + B_\varphi \cdot \hat{e}_\varphi$. Sufficiently far from the light cylinder, the bulk velocity of the jet would be in the poloidal direction. The Lorentz boost on the magnetic field, from the lab frame to the comoving frame, where a fluid element is moving with a Lorentz factor γ_j, exclusively affects the toroidal component, while the poloidal remains unaffected; $b_\varphi = B_\varphi/\gamma_j$ and $b_p = B_p$. However, in our setup, the system is far from axisymmetry and the jets can be offset from the z-axis. Once the jets develop wobbles and the jet axis deviates strongly from a straight line, simplistic assumptions on the morphology of the magnetic field prior to boosting in the fluid frame will lead to the wrong results. To address this hurdle, we first compute the drift velocity of the flow that we use for the Lorentz boost of the magnetic field component perpendicular to that velocity. We define the base vectors $e^i_\parallel$ and $e^i_\perp$ that are parallel and perpendicular to the velocity of the flow, respectively. That way we can write the three-velocity as

$$v^i = v^i_\parallel + v^i_\perp = v_\parallel \cdot e^i_\parallel + v_\perp \cdot e^i_\perp, \tag{A3}$$

where $e^i_\parallel = B^i/B$; $e^i_\perp \cdot B^i = 0$ and B is the magnitude of the lab-frame magnetic field $B^2 = B_i \cdot B^i$, with $B_i = g_{ij}B^j$. As mentioned above, the drift velocity will be perpendicular to the magnetic field component, hence subtracting the parallel component in Equation (A3) we get

$$v_{\rm dr} = v^i - v^i_\parallel = v^i - \frac{(v^j \cdot B_j)B^i}{B^2}, \tag{A4}$$

where $v^i_\parallel = (v^j B_j)B^i/B$ was obtained by multiplying Equation (A3) with B_i/B. After obtaining the spatial components of the drift velocity, we can find the time component of the proper velocity using the relativistic invariant $u^2_{\rm dr} = (u^i \cdot u_i)_{\rm dr} = -1$. Expanding the product, we get

$$-1 = g_{tt}(u^t_{\rm dr})^2 + 2g_{ti}u^t_{\rm dr}u^i_{\rm dr} + g_{ii}(u^i_{\rm dr})^2. \tag{A5}$$

Noting that $\gamma_{\rm dr} = u^t_{\rm dr}$ and $v^i_{\rm dr} = u^i_{\rm dr}/u^t_{\rm dr}$, we can rewrite Equation (A5) as

$$-1 = \gamma^2_{\rm dr} \cdot (g_{tt} + 2g_{ti}v^i_{\rm dr} + g_{ii}(v^i_{\rm dr})^2). \tag{A6}$$

Finally, solving for $\gamma_{\rm dr}$ in Equation (A6), we calculate the fluid-frame magnetic fields as

$$b_{\rm p} \simeq (B^r \cdot B_r)^{1/2}, \tag{A7}$$

$$b_\varphi \simeq \frac{1}{\gamma_{\rm dr}}(B^2 - B^r \cdot B_r)^{1/2}. \tag{A8}$$

Our approximation will hold true as long as (i) we are sufficiently far from the BH ($r \geqslant 10R_{\rm g}$), so that most of the poloidal component is at the r-direction and not in the θ-direction; and (ii) the jets have not developed extreme bends that result in the poloidal component having a significant contribution from the θ- and φ-directions. We argue that in that case, if our goal is to study the growth of the kink instability in the linear regime, this case has ventured into the nonlinear part where our equations should not hold.

Appendix B
AMR Criterion

To identify the jet material, we use a cutoff in a proxy for entropy, $\tilde{S} = u_{\rm g}/\rho^\Gamma$, where $u_{\rm g}$ is the internal energy density, ρ is the comoving frame density of the gas, and $\Gamma = 5/3$ is the gas polytropic index for a monatomic nonrelativistic gas. The reason is that magnetic dissipation in the jets increases the value of $\tilde{S}$, making it appear as "hot." For our run, the cutoff is chosen at $\tilde{S} \geqslant 10$. We additionally refine the cocoons, created when the jets mix with the ambient gas, resulting in a shocked and mildly magnetized gas. The cutoff for the cocoons is chosen at $\tilde{S} \geqslant 0.1$. We also derefine blocks where the jets and/or cocoons left, when the entropy values dropped to $[50\% - 100\%]$ of the cutoff. The AMR criterion is activated once the half-opening angle of either the jets or cocoons becomes narrower than 48 cells (see Gottlieb et al. 2022b), which is the width of a single AMR block, whose resolution is $N^{\rm B}_r \times N^{\rm B}_\theta \times N^{\rm B}_\varphi = 56 \times 48 \times 48$. The maximum effective resolution in the jets can reach $N^{\rm eff}_r \times N^{\rm eff}_\theta \times N^{\rm eff}_\varphi = 3584 \times 768 \times 1536$. This ensures that both the jets and their cocoons are well resolved as they propagate out to large radii: jet opening angles of 0.04 rad $=2.^\circ3$ are resolved with $\geqslant$10 cells out to distances of $5000R_{\rm g}$.

Appendix C
Reduced Scale Separation

For our test run at a reduced scale separation, we use the same physical parameters as in the fiducial run, except we reduce the Bondi-to-event horizon scale separation by 1 order of magnitude, $R_{\rm B}/R_{\rm g} = 10^2$. The grid setup is mostly identical to our fiducial run (see Section 2). However, because we were not interested in the details of the jets, in this case we did not tilt the BH spin 90° with respect to the polar axis. The base grid resolution is the same: $N_r \times N_\theta \times N_\varphi = 448 \times 96 \times 192$ cells in the r-, θ-, and φ-directions. We activate one level of SMR at $r \geqslant 6.5R_{\rm g}$, doubling the resolution in each dimension for an effective resolution $896 \times 192 \times 384$ cells. Figure 8 shows the normalized flux, $\phi_{\rm BH}$, on the BH. The system turns MAD after an unusually long time, at $70\,{\rm k} \lesssim t \lesssim 100\,{\rm k}$, highlighting the importance of long-term simulations.

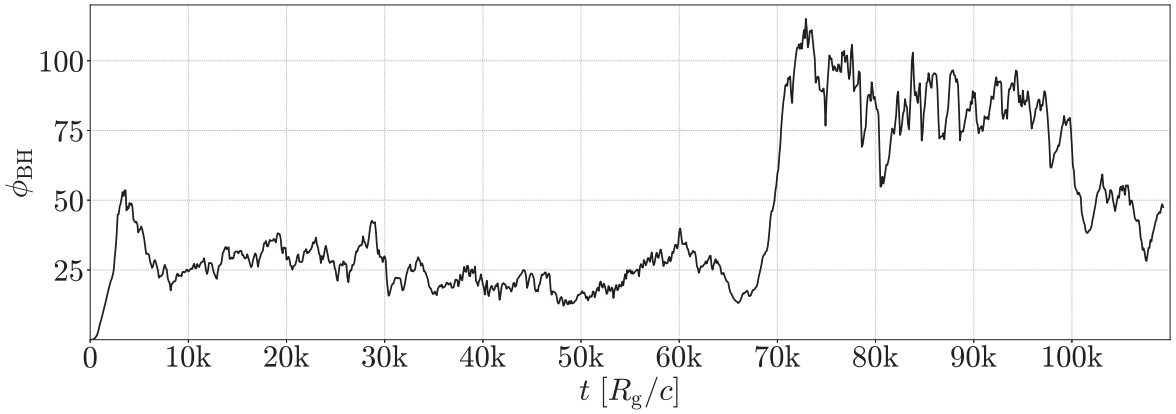

Figure 8. For the reduced scaled separation, $R_{\rm B}/R_{\rm g} = 10^2$, the system turns MAD at 70 k $\lesssim t \lesssim$ 100 k.

ORCID iDs

Aretaios Lalakos https://orcid.org/0000-0002-6883-6520
Alexander Tchekhovskoy https://orcid.org/0000-0002-9182-2047
Omer Bromberg https://orcid.org/0000-0003-4271-3941
Ore Gottlieb https://orcid.org/0000-0003-3115-2456
Jonatan Jacquemin-Ide https://orcid.org/0000-0003-2982-0005
Matthew Liska https://orcid.org/0000-0003-4475-9345
Haocheng Zhang https://orcid.org/0000-0001-9826-1759

References

Ackermann, M., Bustamante, M., Lu, L., et al. 2022, JHEAp, 36, 55
Anglés-Alcázar, D., Faucher-Giguère, C.-A., Quataert, E., et al. 2017, MNRAS, 472, L109
Anglés-Alcázar, D., Özel, F., Davé, R., et al. 2015, ApJ, 800, 127
Anglés-Alcázar, D., Quataert, E., Hopkins, P. F., et al. 2021, ApJ, 917, 53
Balbus, S. A., & Hawley, J. F. 1991, ApJ, 376, 214
Baldi, R. D. 2023, A&ARv, 31, 3
Baldi, R. D., Capetti, A., & Massaro, F. 2018, AA, 609, A1
Balmaverde, B., & Capetti, A. 2006, A&A, 447, 97
Barniol Duran, R., Tchekhovskoy, A., & Giannios, D. 2017, MNRAS, 469, 4957
Bateman, G. 1978, MHD Instabilities (Cambridge, MA: MIT Press)
Begelman, M. C. 1998, ApJ, 493, 291
Biretta, J. A., Stern, C. P., & Harris, D. E. 1991, AJ, 101, 1632
Bisnovatyi-Kogan, G. S., & Ruzmaikin, A. A. 1974, Ap&SS, 28, 45
Bisnovatyi-Kogan, G. S., & Ruzmaikin, A. A. 1976, Ap&SS, 42, 401
Blandford, R. D., & Payne, D. G. 1982, MNRAS, 199, 883
Blandford, R. D., & Znajek, R. L. 1977, MNRAS, 179, 433
Bondi, H. 1952, MNRAS, 112, 195
Bromberg, O., Singh, C. B., Davelaar, J., & Philippov, A. A. 2019, ApJ, 884, 39
Bromberg, O., & Tchekhovskoy, A. 2016, MNRAS, 456, 1739
Chatterjee, K., Liska, M., Tchekhovskoy, A., & Markoff, S. B. 2019, MNRAS, 490, 2200
Cui, Y., Hada, K., Kawashima, T., et al. 2023, Natur, 621, 711
Das, T. K., & Czerny, B. 2012, MNRAS, 421, L24
Davis, S. W., & Tchekhovskoy, A. 2020, ARA&A, 58, 407
Di Matteo, T., Allen, S. W., Fabian, A. C., Wilson, A. S., & Young, A. J. 2003, ApJ, 582, 133
Eichler, D. 1993, ApJ, 419, 111
Fabian, A. C. 2012, ARA&A, 50, 455
Fanaroff, B. L., & Riley, J. M. 1974, MNRAS, 167, 31P
Ghisellini, G. 2011, in AIP Conf. Proc. 1381, 25th Texas Symp. on Relativistic Astrophysics (TEXAS 2010), ed. F. Aharonian, W. Hofmann, & F. Rieger (Melville, N Y: AIP), 180
Giannios, D., Uzdensky, D. A., & Begelman, M. C. 2009, MNRAS, 395, L29
Gottlieb, O., Lalakos, A., Bromberg, O., Liska, M., & Tchekhovskoy, A. 2022a, MNRAS, 510, 4962
Gottlieb, O., Liska, M., Tchekhovskoy, A., et al. 2022b, ApJL, 933, L9
Igumenshchev, I. V. 2008, ApJ, 677, 317
Igumenshchev, I. V., Narayan, R., & Abramowicz, M. A. 2003, ApJ, 592, 1042
Komissarov, S., Vlahakis, N., Konigl, A., & Barkov, M. 2009, MNRAS, 394, 1182
Kwan, T. M., Dai, L., & Tchekhovskoy, A. 2023, ApJL, 946, L42
Lalakos, A., Gottlieb, O., Kaaz, N., et al. 2022, ApJL, 936, L5
Lense, J., & Thirring, H. 1918, PhyZ, 19, 156
Li, Y., Gendron-Marsolais, M.-L., Zhuravleva, I., et al. 2020, ApJL, 889, L1
Liska, M., Chatterjee, K., Issa, D., et al. 2022, ApJS, 263, 26
Lundquist, J. P., Merten, L., Vorobiov, S., et al. 2022, 37th Int. Cosmic Ray Conf. (ICRC2021), ed. A. Kappes & B. Keilhauer, (Trieste: SISSA), 989
Lyubarskii, Y. E. 1999, MNRAS, 308, 1006
Lyubarskij, Y. E. 1992, SvAL, 18, 356
Lyubarsky, Y. 2009, ApJ, 698, 1570
Martizzi, D., Quataert, E., Faucher-Giguère, C.-A., & Fielding, D. 2019, MNRAS, 483, 2465
McKinney, J. C., Tchekhovskoy, A., & Blandford, R. 2012, MNRAS, 423, 3083
McNamara, B., & Nulsen, P. 2007, ARA&A, 45, 117
McNamara, B., & Nulsen, P. 2012, NJPh, 14, 055023
Merten, L., Boughelilba, M., Reimer, A., et al. 2021, APh, 128, 102564
Mizuno, Y., Lyubarsky, Y., Nishikawa, K.-I., & Hardee, P. E. 2009, ApJ, 700, 684
Mizuno, Y., Lyubarsky, Y., Nishikawa, K.-I., & Hardee, P. E. 2012, ApJ, 757, 16
Morganti, R. 2017, FrASS, 4, 42
Narayan, R., Igumenshchev, I. V., & Abramowicz, M. A. 2003, PASJ, 55, L69
Narayan, R., Li, J., & Tchekhovskoy, A. 2009, ApJ, 697, 1681
Narayan, R., Sądowski, A., Penna, R. F., & Kulkarni, A. K. 2012, MNRAS, 426, 3241
Oei, M. S. S. L., van Weeren, R. J., Hardcastle, M. J., et al. 2022, A&A, 660, A2
Paliya, V. S. 2021, ApJL, 918, L39
Perley, R. A., Dreher, J. W., & Cowan, J. J. 1984, ApJL, 285, L35
Ressler, S. M., Quataert, E., White, C. J., & Blaes, O. 2021, MNRAS, 504, 6076
Ressler, S. M., Tchekhovskoy, A., Quataert, E., & Gammie, C. F. 2017, MNRAS, 467, 3604
Russell, H. R., Fabian, A. C., McNamara, B. R., et al. 2018, MNRAS, 477, 3583
Russell, H. R., Fabian, A. C., McNamara, B. R., & Broderick, A. E. 2015, MNRAS, 451, 588
Schoeffler, K. M., Grismayer, T., Uzdensky, D., & Silva, L. O. 2023, MNRAS, 523, 3812
Shapiro, S. L., Lightman, A. P., & Eardley, D. M. 1976, ApJ, 204, 187
Shapiro, S. L., & Teukolsky, S. A. 1986, in Black Holes, White Dwarfs and Neutron Stars: The Physics of Compact Objects, ed. S. L. Shapiro & S. A. Teukolsky (New York: Wiley), 672
Sikora, M., Stawarz, Ł, & Lasota, J.-P. 2007, ApJ, 658, 815
Stecker, F. W., Shrader, C. R., & Malkan, M. A. 2019, ApJ, 879, 68
Tavecchio, F., Righi, C., Capetti, A., Grandi, P., & Ghisellini, G. 2018, MNRAS, 475, 5529

Tchekhovskoy, A. 2015, in The Formation and Disruption of Black Hole Jets, ed. I. Contopoulos, D. Gabuzda, & N. Kylafis (Cham: Springer), 45
Tchekhovskoy, A., & McKinney, J. C. 2012, MNRAS, 423, L55
Tchekhovskoy, A., McKinney, J. C., & Narayan, R. 2009, ApJ, 699, 1789
Tchekhovskoy, A., Narayan, R., & McKinney, J. C. 2010, NewA, 15, 749
Tchekhovskoy, A., Narayan, R., & McKinney, J. C. 2011, MNRAS, 418, L79
Zhuravleva, I., Churazov, E., Arévalo, P., et al. 2016, MNRAS, 458, 2902